EDDY CURRENT DAMPING APPLICATIONS FOR VIBRATION ISOLATION PURPOSES

by

Efe ÖZKAYA

B.S., Mechanical Engineering, Boğaziçi University, 2013

Submitted to the Institute for Graduate Studies in
Science and Engineering in partial fulfillment of
the requirements for the degree of
Master of Science

Graduate Program in Mechanical Engineering
Boğaziçi University

2016

ACKNOWLEDGEMENTS

First of all, I feel myself lucky for having the opportunity to work with Assoc. Prof. Çetin Yılmaz. I am grateful for his endless support, patience and guidance throughout my entire graduate study. This work would not be completed without his contributions. In addition to being an advisor to me, he is also person that I admire in his personal life. I would like to thank him as being a great mentor and a role model to me.

I also acknowledge Assoc. Prof. Veysi Erkcan Özcan for allowing me to use his laboratory and creating spare time to explain theoretical background of certain mathematical calculations which were essential for my research.

I thank Prof. Metin Aydoğdu who accepted to become a member in the thesis jury.

I would like to thank İbrahim Mutlu for his help during the production of prototypes to be used in the measurements.

Finally, I would like to thank my family for their support in every circumstance. I thank my mother, my father and my brother for supporting me to pursue a career in academia. I thank my roommate Erhan and my friend Caitlin for motivating me all the time. I could have not accomplished to finish this research without your support.

This work was supported by Boğaziçi University Research Grant No. 14A06P6 and TÜBITAK Grant No. 110M663.

ABSTRACT

EDDY CURRENT DAMPING APPLICATIONS FOR VIBRATION ISOLATION PURPOSES

In this thesis, passive eddy current damping (ECD) is used in two different novel designs that show vibration stop bands. One includes an inertial amplification mechanism and the other includes local resonators. In both designs, copper tube-ring magnet couple is used as a passive eddy current damper. The reason for such usage arises from the fact that this damping method does not require an external power source and its damping constant can be easily changed. The change in the damping constant is obtained by adjusting the distance between the conducting material which is the copper tube and the magnetic field generator which is the magnet. In the first design, which includes an inertial amplification mechanism, vertical motion is dampened by copper tube-ring magnet couple, which serves as a viscous damping component. For this design, a prototype is produced and experimental measurements are taken to show the effect of damping on vibration amplitudes. In the second design, which includes local resonators, it is aimed to generate a vibration stop band at low frequencies. The effect of ECD on stop band width, resonance peaks and anti-resonance depth on the frequency response results are observed. For comparison purposes, frequency response of this design is obtained analytically, experimentally and numerically. By both of these designs, it is shown that ECD can be used in different structures to attenuate vibrations.

ÖZET

BURGAÇ AKIMI İLE SÖNÜMLE TEKNİĞİNİN TİTREŞİM YALITIMINA YÖNELİK UYGULAMARI

Bu tezde burgaç akımı ile pasif sönümleme tekniği titreşim bant aralığı gösteren iki farklı özgün yapıya uygulanmıştır. Bu yapılardan ilki atalet artırım mekanizması içerirken, ikincisi yerel rezonatör içeren periyodik bir yapı olmuştur. Her iki yapıda da bakır tüp-halka mıknatıs ikilisi pasif sönümleyici olarak kullanılmıştır. Bu sönümleme yönteminin tercih edilmesi harici bir güç kaynağına gerek duyulmaması ve sönüm katsayısının kolayca değiştirilebilmesinden kaynaklanmaktadır. İletken malzeme olan bakır tüp ve manyetik alan üreticisi olan hareket halindeki halka mıknatıs arasındaki mesafe ayarlanarak sönüm katsayısı değiştirilebilmiştir. Atalet artırım mekanizması içeren ilk yapıda, dikey doğrultudaki titreşim genliğinin sönümlenmesi, halka mıknatıs ve bakır tüp ikilisinin viskoz tipi bir sönümleyici işlevi görmesi ile sağlanmıştır. Bu bağlamda üretilen prototip ile yapılan deneysel ölçümlerde sönümlemenin titreşim genliklerine etkisi incelenmiştir. Yerel rezonatör içeren ikinci yapıda, düşük frekanslarda titreşim bant aralığı elde edilmesi hedeflenmiştir. Ayrıca burgaç akımı ile sönümlemenin titreşim bant aralığına, rezonans tepelerine ve anti-rezonans derinliğine etkisi incelenmiştir. Bu prototipin frekans tepki sonucu deneysel, analitik ve sayısal olarak elde edilip karşılaştırılmıştır. Bu iki tasarım vasıtasıyla, burgaç akımı ile sönümlemenin farklı yapılarda titreşim genliklerini azaltmak için kullanılabileceği gösterilmiştir.

TABLE OF CONTENTS

LIST OF FIGURES

LIST OF TABLES

LIST OF SYMBOLS

B_r	Remanance
B_z	Magnetic field of the magnet on the axis-of-symmetry
c	Damping constant
E	Young's modulus
F_i	Field transfer matrix
$F_{Lorentz}$	Lorentz force
g	Gravitational acceleration
h	Height of a magnet
I	Electrical current
I_o	Moment of inertia
k	Spring stiffness
k_{eq}	Equivalent stiffness
l	Length
L	Lagrangian
l_i	Length of the i^{th} section
m	Mass
m_a	Point mass attached to the lumped parameter model
m_B	Dipole moment of the magnet
m_{eff}	Effective mass
m_i	Mass of the i^{th} section
n	Number of peaks
N	Internal force
P	Power
P_i	Point transfer matrix
q	Point monopole
r	Radius
R	Ohmic resistance
t	time

T	Kinetic energy
t_i	Thickness of the i^{th} section
T_{period}	Period
TR	Transmissibility
u	Displacement
u_h	Horizontal displacement
u_v	Vertical displacement
$U_{overall}$	Overall transfer matrix
v	Velocity
V	Potential energy
w	Width
w/	With
w/o	Without
z	Lumped parameter output displacement
z_h	Distance above the magnet surface
$\underline{z_i}$	State vector
z_0	Lumped parameter input displacement
γ	Wave number
ε	Electromotive force
δ_{log}	Logarithmic decrement
δ_t	Copper wall thickness
ζ	Damping ratio
θ	Lumped parameter model angular coordinate
μ_0	Permeability of free space
ρ	Electrical resistivity
σ	Conductivity
σ_M	Magnetization
Φ	Magnetic flux
ω	Angular frequency

LIST OF ACRONYMS/ABBREVIATIONS

1D	One Dimensional
2D	Two Dimensional
ECD	Eddy Current Damping
FEA	Finite Element Analysis
FEM	Finite Element Model
TMD	Tuned Mass Damper

1. INTRODUCTION

The repetitive motion disturbing the equilibrium position of an object in a time interval is called vibration or oscillation [1]. It occurs in various dynamic systems leading to dynamic stresses that can cause failure [2]. Damping is used to avoid such failures caused by this repetitive motion. It is the mechanism behind the conversion of kinetic energy to heat [3, 4].

1.1. Passive and Active Damping

In dynamic systems, unless resonance could be avoided by design, damping is used to decrease the amplitude of free oscillations [5]. There are two types of damping, which are used to control such unpleasant motions, active and passive damping. In active damping, dissipation of energy from the system is achieved by external means, such as a controlled actuator. Sensors are used to measure the response at each instant and actuators are used to automatically apply forces which oppose the measured vibration response in prescribed manner. In passive damping, dissipation of energy from the system is accomplished by add-on damping devices such as isolator, structural joints and supports, or structural member's internal damping [3, 6].

Examples of passive damping mechanisms include Coulomb or dry friction damping, viscoelastic materials, viscous fluids, magnets, smart materials, high damping alloys, and particle damping. Among them magnet usage can be considered as eddy current damping. This mechanism utilizes the interaction between the generated magnetic field (usually from a strong permanent magnet) and eddy currents induced in a solid conductor, which is attached to the vibrating object, moving inside this magnetic field [7]. The resistive force caused via this damping method is proportional to velocity of the conductor. Thus, it can be considered as a viscous-like damping force.

1.1.1. Eddy Current Damping

Eddy currents are formed when a moving non-magnetic conductor intersects a stationary magnetic field, or vice-versa [8,9]. Circulating eddy currents inside the non-magnetic conductor induce their own magnetic field with the opposite polarity of the applied field that causes a resistive force. Since the resistive force induced by eddy currents is proportional to the relative velocity, the conductor and the magnet can be allowed to function as a type of viscous damping [10, 11]. The use of eddy currents for damping of dynamic systems has been known for decades and its applications are various.

Damping effect caused by the permanent magnet moving on an infinite conducting sheet is investigated in [12]. The theoretical model for the eddy current damper is derived by using the electromagnetic theory combined with the image method. In this model, effect of surface charges on the eddy current damping (ECD) force is taken into consideration. In the case of finite conducting sheet, instead of using infinite imaginary eddy currents, one pair (left and right imaginary eddy currents) is considered to obtain the net eddy current density.

A non-contacting passive damper shown in Figure 1.1 is proposed by [13] to dampen the transverse vibrations of a beam. The beam's motion is in line with the poling axis of the magnet. Experimental and numerical validations are done for the permanent magnet being positioned at numerous distances from the conducting plate attached on the beam's surface to show the damping effect.

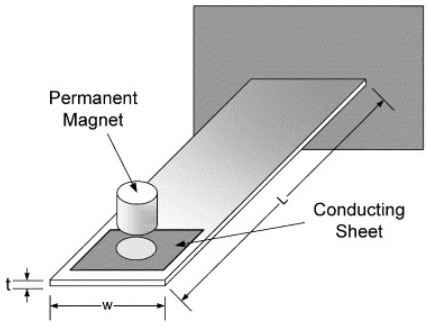

Figure 1.1. Cantilever Beam in Magnetic Field Generated by Permanent Magnet [13].

In [14], ECD is used in a magnetic levitation system to enhance the levitation precision of miniaturized objects. Undesired vibrations are suppressed via ECD introduced through a non-ferromagnetic plate being placed beneath the levitated magnet as shown in Figure 1.2.

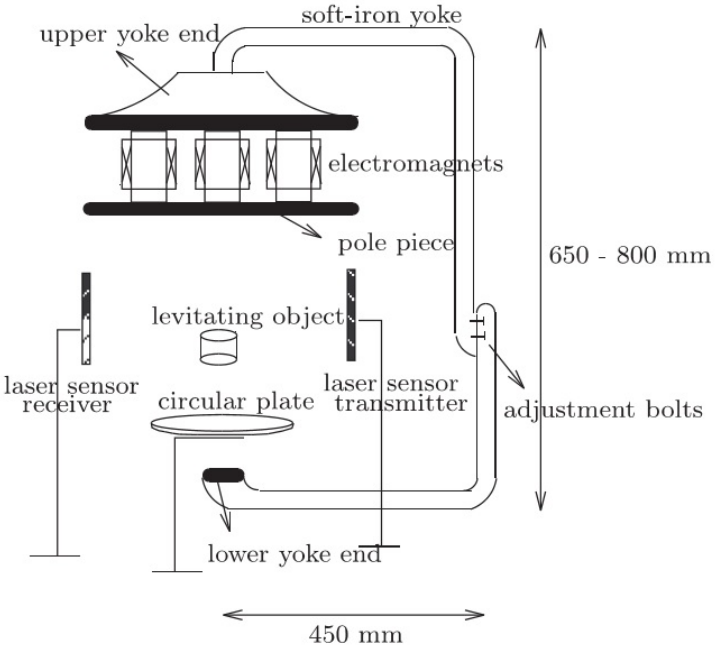

Figure 1.2. Schematic of the Magnetic Levitation Syste [14].

Two cylindrical magnets whose like poles are in close proximity and a ring-shaped conductive aluminium plate are used in [15]. Both spring and variable damping effect are generated by utilizing these components in the design shown in Figure 1.3.

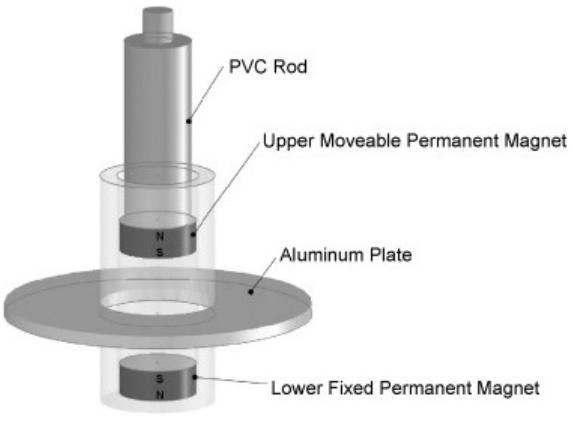

Figure 1.3. Schematic View of the Magnetic Shock Absorber [15].

Another design made by [16] consists of a classical tuned mass damper (TMD) with ECD as seen in Figure 1.4. Magnetically TMD is introduced to improve the damping performance of the conventional TMD by using ECD.

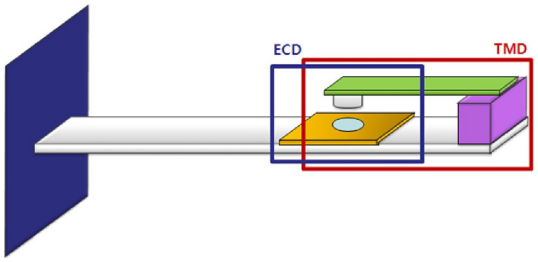

Figure 1.4. Schematic of the Magnetic Tuned Mass Damper [16].

[17] proposed a new type of eddy current damper given in Figure 1.5 with remarkably high efficiency and compactness. Magnetic field is split into multiple ones to reduce the electrical resistance of the eddy current loops and to increase the damping force and damping coefficient.

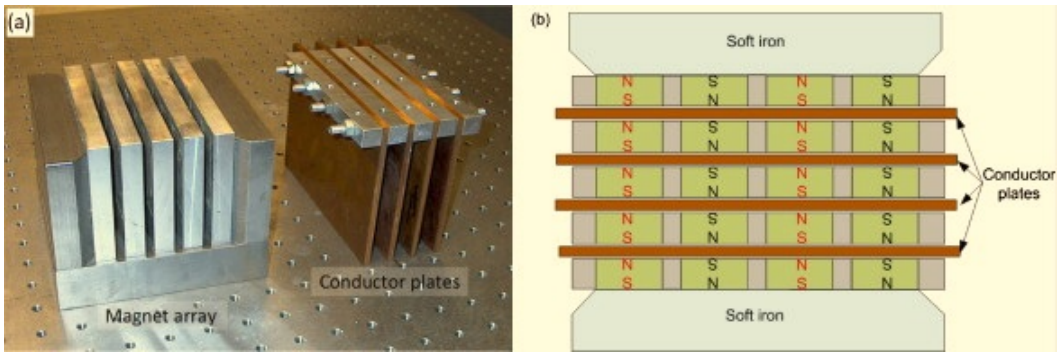

Figure 1.5. Assemblies of Magnetic Array and Conductor Plates and Their Top View [17].

In [18], to overcome the disadvantages of viscous dampers embedded to TMDs, ECD is introduced. It is demonstrated that by varying the air gap between permanent magnets and conductive plates damping ratio can be adjusted. In Figure 1.6, one of the magnetic configurations is given for the proposed TMD with ECD included.

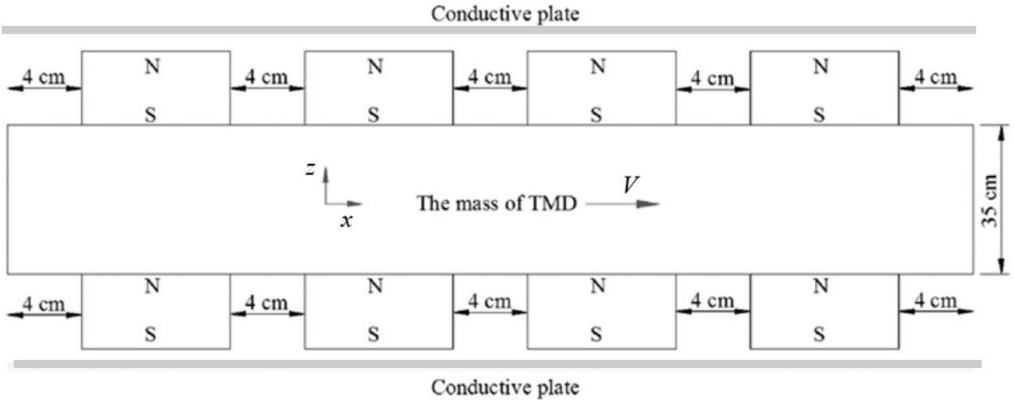

Figure 1.6. Magnet Position Configuration of the Magnetic Tuned Mass Damper [18].

It is targeted in this research to use ECD with two of the band gap generating methods which are local resonances and inertial amplification. ECD is used for the first time with these methods and its effect on the frequency response is investigated.

1.2. Band Gap Generation Methods

The theory of wave propagation in periodic structures was developed by solid state physicists and electrical engineers several decades ago. In the last two decades, prevention of propagation of acoustic or elastic waves in certain frequency ranges via periodic materials and structures received considerable attention. The frequency ranges where the vibration is suppressed can be considered as phononic band gap in infinitely periodic case. [19] investigated the vibrational response of the finite case subjected to periodic loading. For this case, frequency ranges where the vibration is suppressed can be considered as stop bands.

Three different methods are presented to generate phononic band gaps that hinder the wave propagation in certain frequency ranges. They are called Bragg scattering, local resonances and inertial amplification.

In Bragg scattering, reflected waves from the heavy inclusions in a soft media are the cause of the band gap generation. In order to have a band gap at low frequencies,

low wave speed and large lattice constant are required in this method. A mass-spring system, shown in Figure 1.7, is used to demonstrate a one-dimensional (1D) periodic structure which uses Bragg scattering method to generate band gap.

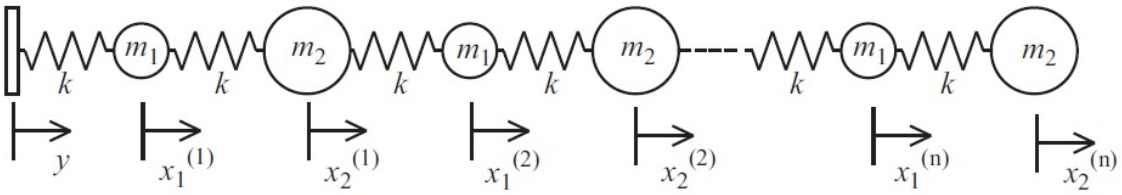

Figure 1.7. Mass Spring Array to Induce a Band Gap via Bragg Scattering [20].

There is another method called local resonances (Resonance Scattering) which can also induce band gaps by blocking wave propagation nearby the resonance frequencies of the resonators [21–23]. This method extracts the energy of the propagating wave when the attached resonators get excited around their resonance frequencies. To obtain wide band gaps at low frequencies via this method, large volume filling fractions are required [24–26]. Large weight and size are not good attributes for band gap structures that are to be used for practical purposes. Sketch of a system with local resonators attached to each unit cell is given in Figure 1.8.

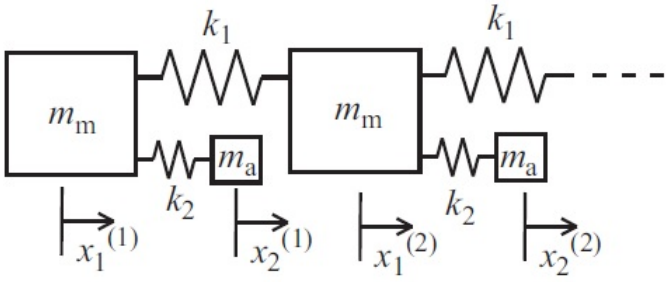

Figure 1.8. Resonators Attached to Each Unit Cell to Induce a Band Gap via Resonance Scattering [20].

To avoid the short comings of the previous methods inertial amplification is proposed in [27]. In the inertial amplification method, the mass m is attached to the

output end of a displacement amplification mechanism. As the two ends of the mechanism move with respect to each other, mass m_a moves with large amplitude if θ is small. As a result, large effective inertia is achieved. It is shown that this method gives rise to very wide band gaps at low frequencies with fewer unit cells compared to the previous methods [28, 29]. A 1D array of inertial amplification mechanism is shown in Figure 1.9.

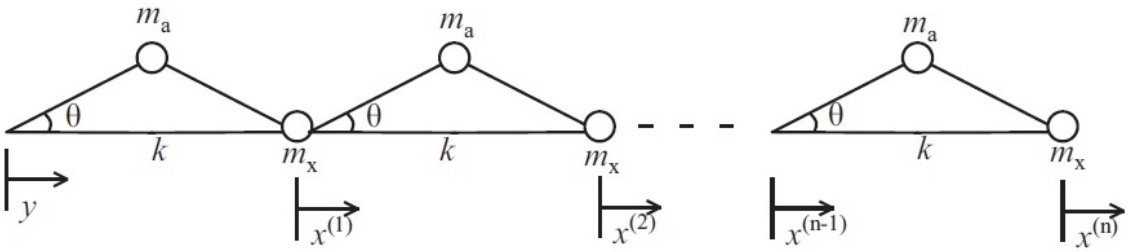

Figure 1.9. 1D Array of Inertial Amplification Mechanisms [20].

In finite periodic structures, the frequencies where sharp attenuation occurs are known as anti-resonance frequencies. Generally, anti-resonance frequencies in a structure can be created by local resonance and inertial amplification method. Both methods are capable of generating low-frequency band gaps in finite and infinite periodic structures.

1.3. Motivation and Research Objective

In this research, implementation of ECD to an inertial amplification mechanism involving structure is targeted. Furthermore, embedding ECD into a locally resonant periodic structure is aimed. Motivations behind this research can be summarized as

- Using ECD that does not require any external power source as a non-contact damping method which does not wear due to friction as other viscous damping methods.
- Building two novel structures in which vibration attenuation is accomplished via ECD usage.

- Observing the effect of ECD on the generated frequency response results through an inertial amplification mechanism including structure.
- Generating a stop band at low frequencies through a locally resonant periodic structure to hinder the 1D axial wave propagation.

ECD is embedded into the four legged inertial amplification mechanism to observe its effect on resonance peaks and anti-resonance depth. This is followed by inclusion of ECD into a locally resonant periodic structure to generate stop band at low frequencies. The inclusion of ECD to these structures are accomplished through the relative motion in between a ring magnet and a copper tube.

2. INERTIAL AMPLIFICATION MECHANISM

The lumped parameter model of the inertial amplification mechanism used in this thesis is composed of two rigid links connected directly from one end with an attached point mass (m_a), and connected via spring and damper from the other end as shown in Figure 2.1.

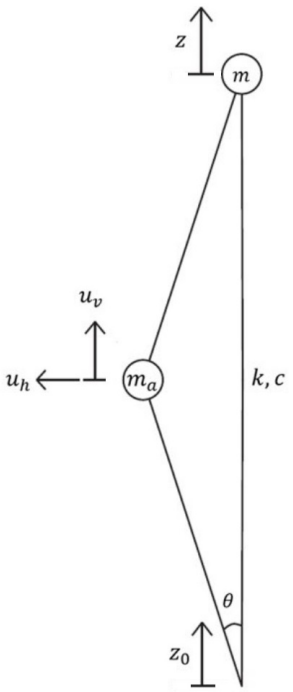

Figure 2.1. Sketch of the Lumped Parameter Model of the Inertial Amplification Mechanism.

For small θ values, the displacement of the ends of the spring is amplified through the mechanism, and the displacement of the point mass is greater for smaller θ values. The relation between the end displacements and the displacement of the point mass is given in Equation 2.1 and Equation 2.2.

$$u_v = \frac{z_0 + z}{2} \tag{2.1}$$

$$u_h = \frac{z_0 - z}{2} \cot\theta \tag{2.2}$$

where u_v is the vertical and u_h is the horizontal displacement of the attached point mass. The potential energy (V) and the kinetic energy (T) of the lumped parameter model shown in Figure 2.1 are given in Equation 2.3 and Equation 2.4, respectively.

$$V = \frac{1}{2}k(z - z_0)^2 \tag{2.3}$$

$$T = \frac{1}{2}m_a \left(\left(\frac{\dot{z_0} + \dot{z}}{2} \right)^2 + \left(\frac{\dot{z_0} - \dot{z}}{2} \cot\theta \right)^2 \right) + \frac{1}{2}m\dot{z}^2 \tag{2.4}$$

where k is the spring constant. Moreover, Rayleigh Dissipation Function ($\widetilde{F}$) can be found as

$$\widetilde{F} = \frac{1}{2}c(\dot{z} - \dot{z_0})^2 \tag{2.5}$$

where c is the damping constant. Equation of motion of the lumped parameter model given in Equation 2.7 is found through Lagrange Method shown in Equation 2.6 where $L = T - V$

$$\frac{d}{dt}\left(\frac{\partial L}{\partial \dot{z}}\right) - \frac{\partial L}{\partial z} = Q, \qquad Q = \frac{-d\widetilde{F}}{d\dot{z}} \tag{2.6}$$

$$\left(\frac{1}{2}m_a(1 + \cot\theta) + m\right)\ddot{z} + c\dot{z} + kz = \left(\frac{1}{2}m_a(\cot\theta - 1)\right)\ddot{z_0} + c\dot{z_0} + kz_0 \tag{2.7}$$

The effective mass ($m_{eff} = \frac{1}{2}m_a(1 + \cot\theta) + m$) and the equivalent stiffness ($k_{eq} = k$) of the model is obtained to be used in damping constant calculation.

2.1. Distributed Parameter Model

A distributed parameter model, first mode of which is equivalent to the lumped parameter model, is designed. The isometric and side view of this distributed parameter model can be seen in Figure 2.2. This model is a single branch of a four legged design in which ECD is not included, yet.

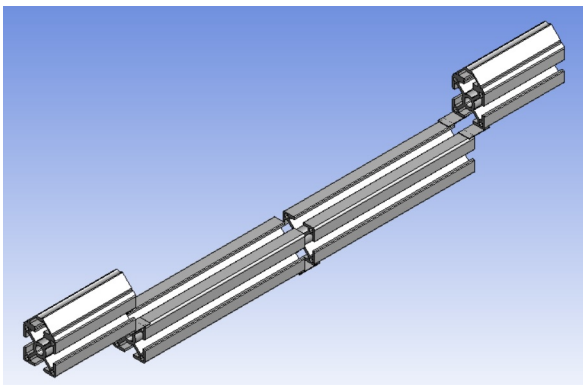

(a)

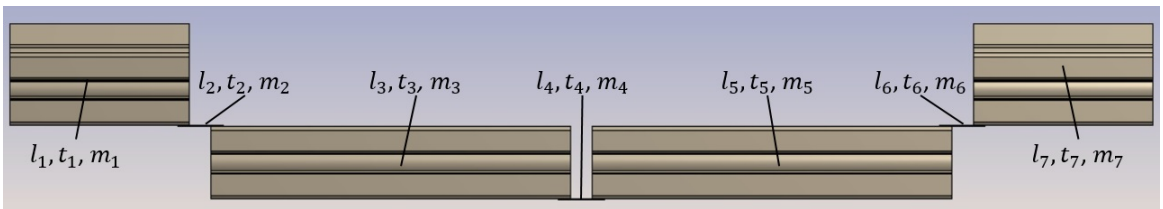

(b)

Figure 2.2. (a) Isometric View and (b) Side View of the Distributed Parameter Model of a Single Branch of the Four Legged Design. Here, l_i, t_i and m_i are the Length, Thickness and Mass of the i^{th} Section that Forms the Structure.

First mode shape of this distributed parameter model for a single branch is given in Figure 2.3 in which both ends are free to move vertically. The equivalent stiffness (k_{eq}) and the effective mass (m_{eff}) of the four legged structure is obtained through the calculation of the kinetic and potential energy of this single branch's first mode shape.

Relative vertical displacements of the two ends of beam section 2, section 3 and the half of the beam section 4 in the middle part of the single branch are given in Equations 2.8−2.10 respectively and shown in Figure 2.3. Length, thickness and mass

of beam sections 1 and 7, beam sections 2, 4, and 6 and beam sections 3 and 5 are equal.

$$z_1 = l_2 \left(1 - \frac{\sin\theta}{\theta}\right) \tag{2.8}$$

$$z_2 = l_3(1 - \cos\theta) + (t_3 + t_2)\sin\theta \tag{2.9}$$

$$z_3 = \frac{l_2}{2}\left(1 - \frac{\sin\theta}{\theta}\right) \tag{2.10}$$

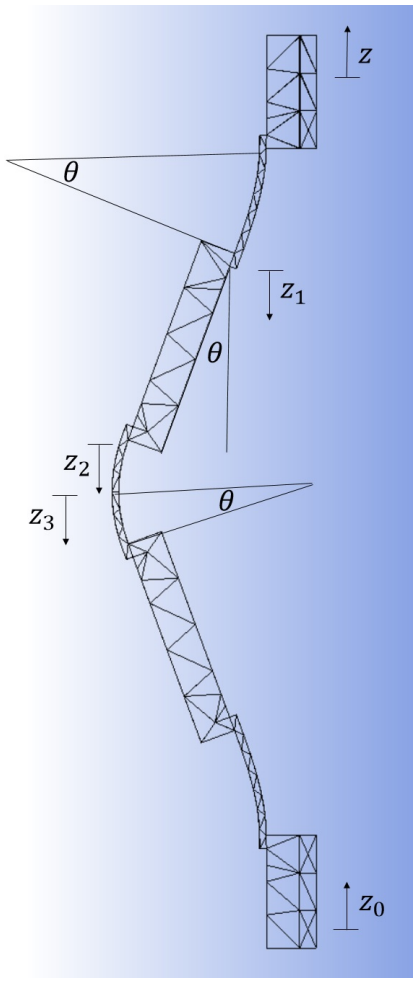

Figure 2.3. Sketch of the Distributed Parameter Model of a Single Branch of the Four Legged Design.

The relative displacement between the bottom and the top parts is given in Equation 2.11.

$$z_0 - z = 2(z_1 + z_2 + z_3) \tag{2.11}$$

Assuming angular displacements are small by inserting $\sin\theta = \theta$ and $\cos\theta = 1$ into Equation 2.11, the relative displacement of the bottom portion with respect to the top part can be found in terms of the angular displacement, as

$$z_0 - z = 2(t_3 + t_2)\theta \tag{2.12}$$

Through equating the potential energy of the distributed parameter model (Equation 2.13) [20] to the lumped parameter model (Equation 2.14) k_{eq} is obtained as in Equation 2.15.

$$V_{distributed} = \frac{24EI_2\theta^2}{l_2} \tag{2.13}$$

where I_2 is the moment of inertia and E is the Young's Modulus.

$$V_{lumped} = \frac{1}{2}k(z - z_0)^2 = 2k(t_3 + t_2)^2\theta^2 \tag{2.14}$$

$$k_{eq} = \frac{12EI_2}{l_2(t_3 + t_2)^2} \tag{2.15}$$

Beam sections 2, 4, and 6, which are flexible connections, are considered to have negligible mass. Thus, the kinetic energy of the system is calculated by considering the rotational and linear motion of sections 3 and 5, and the linear motion of section 1 and 7. To calculate the rotational kinetic energy of the sections 3 and 5, mass

moment of inertia of them with respect to the center of mass of sections 2 and 6 are calculated, respectively as given in Equation 2.16 by using the parallel axis theorem. Mass moments of inertia (I_0) of sections 3 and 5 are the same.

$$I_0 = m_3\left(\frac{t_3^2 + l_3^2}{12}\right) + m_3\left(\left(\frac{l_3 + l_2}{2}\right)^2 + \left(\frac{t_3 + t_2}{2}\right)^2\right) \tag{2.16}$$

Total rotational kinetic energy (T_r) including four pieces of section 3 and four pieces of section 5 is given in Equation 2.17.

$$T_r = \frac{I_0(\dot{z_0} - \dot{z})^2}{(t_3 + t_2)^2} \tag{2.17}$$

Translation of the center of mass of the four pieces of section 3 and four pieces of section 5 with masses m_3 and m_5 is $(z + z_0)/2$. Thus, the total translational kinetic energy (T_t) of four pieces of section 3, four pieces of section 5, four pieces of section 1 and four pieces of section 7 is given in Equation 2.18. Equation 2.18 will be modified when ECD is included to the structure since the mass under translational motion will change.

$$T_t = m_3(\dot{z} + \dot{z_0})^2 + 2m_1\dot{z}^2 + 2m_7\dot{z_0}^2 \tag{2.18}$$

As a result, the total kinetic energy of the mechanism is

$$T = T_r + T_t = \frac{I_0(\dot{z_0} - \dot{z})^2}{(t_3 + t_2)^2} + m_3(\dot{z} + \dot{z_0})^2 + 2m_1\dot{z}^2 + 2m_7\dot{z_0}^2 \tag{2.19}$$

The equation of motion is written using the Lagrange Method given in Equation 2.6. Lagrange's equation for the distributed parameter model for the z coordinate is

given as follows:

$$\frac{d}{dt}\left(\frac{\partial L}{\partial \dot{z}}\right) - \frac{\partial L}{\partial z} = \frac{d}{dt}\left(\frac{\partial T}{\partial \dot{z}}\right) + \frac{\partial V}{\partial z} = \frac{-d\widetilde{F}}{d\dot{z}} \tag{2.20}$$

Equation of motion given in Equation 2.21 is found by inserting the potential energy given in Equation 2.14 and the total kinetic energy given in Equation 2.19 into Equation 2.20.

$$\left(\frac{2I_0}{(t_3+t_2)^2} + 2m_3 + 4m_1\right)\ddot{z} + c\dot{z} + k_{eq}z = \left(\frac{2I_0}{(t_3+t_2)^2} - 2m_3\right)\ddot{z_0} + c\dot{z_0} + k_{eq}z_0 \tag{2.21}$$

Notice that the term which multiplies $\ddot{z}$ in Equation 2.21 is the effective mass of this system,

$$m_{eff} = \frac{2I_0}{(t_3+t_2)^2} + 2m_3 + 4m_1 \tag{2.22}$$

As mentioned before, effective mass formula given in Equation 2.22 will be modified because of the mass change in beam section 1 caused by the inclusion of ECD.

2.2. Eddy Current Damping Inclusion

The most widely known example of eddy currents for demonstration purposes is "Drag on a Magnet Falling Down a Conductive Tube" [30–33]. Dropping a magnet down the tube as it falls nearly with a constant velocity gives a remarkable manifestation of the reality of eddy currents. In [34, 35] the effect of the number of magnets, the tube's wall thickness, and the offset between the magnet's and the tube's symmetry axes on induced eddy currents have been investigated.

In this part of the research, eddy currents are induced by the relative motion of a ring magnet attached to the vibrating object with respect to the stationary copper tube. Damping coefficient of this viscous type of damper is obtained experimentally, analytically and numerically.

2.2.1. Analytically Obtained Damping Constant

Calculation of the damping constant of a permanent magnet moving through a conductive tube was the focus of numerous studies so far [36–39]. By modeling the magnetic field of the falling magnet as a dipole and assuming that the magnet height is small compared to its diameter, the terminal velocity of the falling cylindrical magnet through a conductive cylindrical tube can be found as [40, 41]

$$v_{terminal} = \frac{128(mg)(8r_{mean}^4)}{45\sigma\delta_t\mu_0^2 m_B^2} \tag{2.23}$$

where μ_0 is the permability of the free space, m_B is the magnetic dipole moment of the magnet, δ_t is the wall thickness of the tube, σ is the conductivity of the tube, r_{mean} is the mean radius of the tube, and mg is the weight of the magnet. The only unknown, magnetic dipole moment is calculated by using Equation 2.24 and 2.25 [40] with remanence (B_r) value for N35 type magnet taken as 1.17 T.

$$B_z(z) = \frac{B_r}{2}\left(\frac{h_c + z}{\sqrt{r_c^2 + (h_c + z)^2}} - \frac{z}{\sqrt{r_c^2 + z^2}}\right) \tag{2.24}$$

In Equation 2.24, h_c is the cylindrical magnet's height, r_c is its radius and z is the distance above from the surface center. Table 2.1 shows the Gaussmeter measurements and the calculated magnetic field values by Equation 2.24. It is seen that measured and calculated values show quite good match, which validates the reliability of the formula given in 2.24 for the cylindrical magnet.

Table 2.1. Measured and Calculated $B_z(z)$ Values

Distance above surface (mm)	Measurement values (mT)	Calculated values (mT)
0	404	410
20	73	71
25	46	47
30	32	33
35	23	23
40	18	17
45	13	13
50	10	10

In Equation 2.25, the axial magnetic field due to dipole approximation is given [41].

$$B_z(z) = \frac{2\mu_0 m_B}{4\pi z^3} \tag{2.25}$$

If the magnetic field values for several points above the magnet's surface on the axis of symmetry through Equation 2.24 are calculated and then by equating these values with Equation 2.25, several magnetic dipole moments can be found. Afterwards, with the most suitable magnetic dipole moment, terminal velocity can be calculated for the cylindrical magnet.

In order to use Equation 2.23 for a ring magnet, principle of superposition can be applied as given in Figure 2.4.

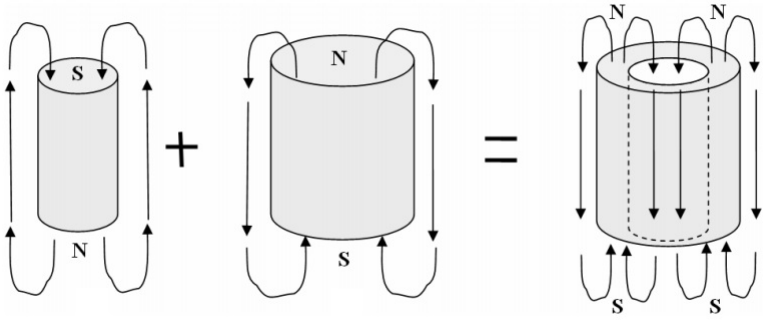

Figure 2.4. Superposition of Two Concentric Cylindrical Magnets [42].

For the ring magnet used in experimental measurements whose dimensions are given in Table 2.2, superposition of two cylindrical magnets with same height differing in radius can be done.

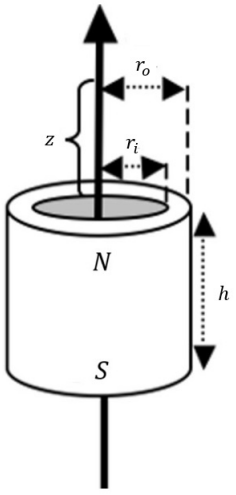

Figure 2.5. Ring Magnet's Magnetic Field on the Axis-of-Symmetry.

For the ring magnet shown in Figure 2.5, the magnetic field formula in Equation 2.24 can be modified as in [43]

$$B_z = \frac{B_r}{2}\left(\frac{h_r+z}{\sqrt{r_o^2+(h_r+z)^2}} - \frac{z}{\sqrt{r_o^2+z^2}} - \frac{h_r+z}{\sqrt{r_i^2+(h_r+z)^2}} + \frac{z}{\sqrt{r_i^2+z^2}}\right) \quad (2.26)$$

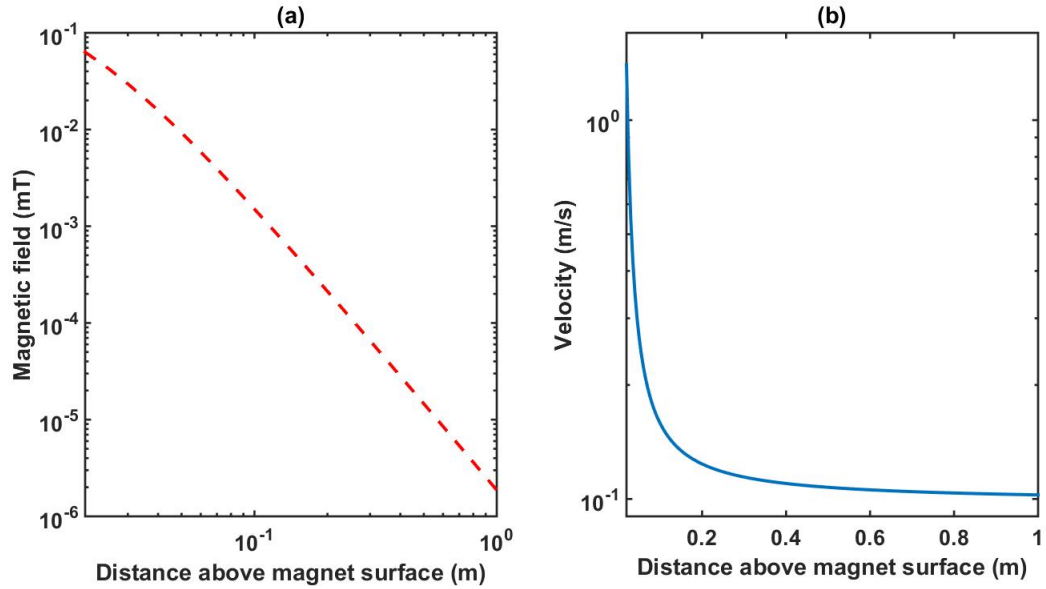

Figure 2.6. (a) Ring Magnet's Magnetic Field on the Axis-of-Symmetry above the Top Surface, (b) Corresponding Terminal Velocity.

The magnetic fields and corresponding terminal velocities for various distances above the top surface area of the ring magnet is given in Figure 2.6. For the ring magnet whose dimensions are given in Table 2.2 that falls through a copper tube with a mean radius (r) of 16.35 mm, wall thickness (δ_t) of 1.5 mm,and conductivity (σ) of $5.88 \times 10^7 \Omega^{-1}\text{m}^{-1}$, $v_{terminal}$ approaches to 0.103 m/s when Equation 2.23 is used. By dividing the magnet weight to this terminal velocity, damping constant found by the dipole approximation ($c_{ana-dipole}$) can be calculated as 7.18 kg/s.

Since in short amount of time, velocity becomes constant for a falling magnet inside a copper tube, it can be assumed that the magnet moves with constant velocity. Its kinetic energy does not change and the gravitational potential energy is transformed into the ohmic heating of the copper tube. In steady state, the rate of gravitational energy lost by the magnet is equal to the rate of the energy dissipation by the ohmic resistance (R),

$$mgv_{terminal} = \sum_z I(z)^2 R \tag{2.27}$$

where I is the electrical current.

Using the terminal velocity calculations done for the cylindrical magnet in [44] a similar formula for the magnetic flux Φ_{total} can be derived for a ring magnet as given in Equation 2.28 assuming that the ring magnet has uniform magnetization.

$$\Phi_{total} = \Phi_o - \Phi_i = \frac{\mu_0}{2}\left(\frac{z+h}{\sqrt{(z+h)^2 + r_{internal}^2}} - \frac{z}{\sqrt{z^2 + r_{internal}^2}}\right)(q_o - q_i) \qquad (2.28)$$

where Φ_o and Φ_i represents the magnetic flux on copper rings generated by cylindrical magnets with radius r_o and r_i, respectively. For both magnets, the heights (h) are the same. $r_{internal}$ is the internal radius of the copper tube. By subtracting Φ_o from Φ_i the magnetic flux generated on a copper ring by a ring magnet is acquired. $q_o = \pi r_o^2 \sigma_{M-o}$ and $q_i = \pi r_i^2 \sigma_{M-i}$ are the representations of charge disks which are the top and bottom surfaces of the cylindrical magnets, as point monopoles having the same net charge as the disks. It is assumed that the magnets have uniform magnetization $\mathbf{M}$=M$\widehat{z}$. That is the effective magnetic charge density inside each magnet is zero, and effective magnetic charge density σ_M vanishes on the side of the magnet and is $\pm M$ on the top and bottom.

As the magnet falls, the flux through each copper ring changes, which results in an electromotive force given by Faraday's law,

$$\varepsilon(z) = -\frac{d\Phi_{total}(z)}{dt} \qquad (2.29)$$

and an electrical current

$$I(z) = \frac{\mu_o (q_o - q_i) r_{internal}^2 v_{terminal}}{2R} C \qquad (2.30)$$

The rate of energy dissipation can be calculated by evaluating the sum on the right-hand side of Equation 2.27. By taking the continuum limit, we find the power

(P) dissipated to be

$$P = \frac{\mu_o^2 (q_o - q_i)^2 r_{internal}^4 v_{terminal}^2}{4R} \int_{-\infty}^{\infty} \frac{C^2}{l} dz \tag{2.31}$$

where $C = \frac{1}{(z^2+r_{internal}^2)^{3/2}} - \frac{1}{((z+h)^2+r_{internal}^2)^{3/2}}$.

The resistance of each copper tube is $R = 2\pi r_{internal}\rho/(\delta_t l)$, where ρ is the electrical resistivity, δ_t is the copper wall thickness and l is the copper tube length.

For the uniform magnetization approximation, the value for σ_M can be found by using Equation 2.32 on the axis of symmetry as

$$\sigma_{M-o} = \frac{2B_o\sqrt{h^2 + r_o^2}}{\mu_0 h} \tag{2.32}$$

for the large magnet and

$$\sigma_{M-i} = \frac{2B_i\sqrt{h^2 + r_i^2}}{\mu_0 h} \tag{2.33}$$

for the small magnet.

By calculating the surface magnetic field (B) values on the axis of symmetry for both of these cylindrical magnets, q_{large} and q_{small} are obtained be used in Equation 2.31. Substituting Equation 2.31 into Equation 2.27, $v_{terminal}$ can be found as 0.111 m/s and by dividing the magnet weight to this terminal velocity, damping constant found by the power dissipation method $(c_{ana-power})$ can be obtained for the ring magnet as 6.77 kg/s.

2.2.2. Numerically Obtained Damping Constant

A finite element model (FEM) is created by COMSOL-Multiphysics 4.3b as given in Figure 2.7 for the ring magnet whose dimensions are given in Table 2.2. Through the

analysis of this numerical model, terminal velocity of the magnet ($v_{terminal}$) is found as 0.054 m/s (see Figure 2.7 (e)). Since $v_{terminal}$ is reached in short duration (less than 0.05 seconds according to our FEM analysis), by Equation 2.34 the damping constant of the cylindrical magnet can be obtained.

$$mg = cv_{terminal} \tag{2.34}$$

where m represents the mass of the falling magnet, g represents the earth's gravity, and c is the damping constant. Consequently, the damping constant ($c_{numerical}$) is found to be 13.45 kg/s.

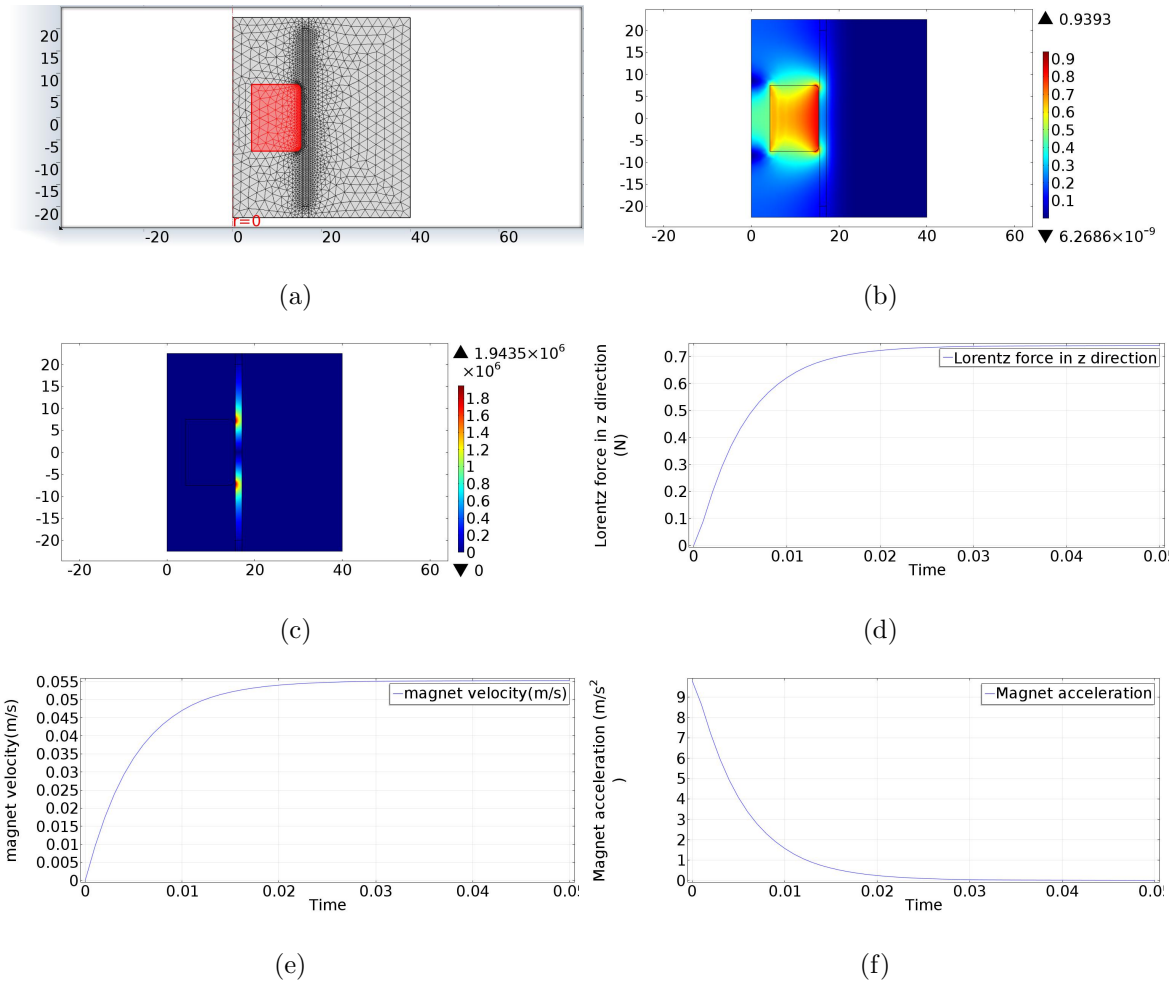

Figure 2.7. (a) 2D Axi-Symmetric FEM of the Copper Tube and the Ring Magnet, (b) Magnetic Flux Density Norm (T) Contour Plot, (c) Current Density Norm (T) Contour Plot, (d) Lorentz Force Acting on the Ring Magnet, (e) Velocity Profile of the Ring Magnet, (f) Acceleration Profile of the Ring Magnet

2.2.3. Experimentally Obtained Damping Constant

2.2.3.1. Free Fall Experiment for Damping Constant Estimation. The basic free fall of a cylindrical magnet through a conducting tube experiment given in Figure 2.8 is done to obtain the damping constant. In this experiment, the copper tube's length, inner radius, wall thickness, and conductivity are 600 mm, 15.6 mm, 1.5 mm, and 5.88×10^7 $1/\Omega.m$ respectively. Terminal velocity is calculated by dividing the length of the copper tube with the measured time of fall with a digital chronometer. Average of 10 free fall experiments are used and standard deviations are calculated. The same set of experiments is performed for a ring magnet, too. Experimentally obtained values of $v_{terminal}$ and c are given in Table 2.2.

Table 2.2. Calculated Velocity and Damping Constant for the Given Ring Magnet.

	Cylindrical Magnet	Ring Magnet
Magnet Height (mm)	10	15
Magnet Inner Radius (mm)	–	4.25
Magnet Outer Radius (mm)	15.35	15.35
Magnet Weight (N)	0.667	0.740
Free Fall Time (s)	8.69 ± 0.096	10.16 ± 0.111
Terminal Velocity (m/s)	0.069	0.059
Damping Constant (kg/s)	9.67	12.5

Figure 2.8. Measurement of the Time of Magnet Fall Inside the Copper Tube.

2.2.3.2. Production of the Prototype. Aluminium beams, fasteners and spring steels are used to design the four legged inertial amplification mechanism. The structure produced is shown in Figure 2.9 and the dimensions and masses of its parts are given in Table 2.3. A ring magnet is used to add the ECD effect to this structure. The ring magnet is fixed to the tip of a threaded rod that passes through the axis of symmetry of the four legged structure. The height of the ring magnet relative to the copper tube can be adjusted by rotating the threaded rod. When the copper tube, situated at the bottom part of the structure, interacts with the ring magnet, ECD effect is observed.

Table 2.3. Design Parameters for the Inertial Amplification Mechanism.

w (m)	0.009
E (N/m^2)	210×10^9
t_2 (m)	0.0005
l_2 (m)	0.009
t_3 (m)	0.030
l_3 (m)	0.150
m_1 (kg)	0.265
m_3 (kg)	0.126

When the threaded rod, copper tube and ring magnet is included to the system Equation 2.22 needs to be modified due to the additional translational kinetic energy caused by the added parts to the system. Since the copper tube is attached to beam section 7, just the masses of ring magnet and threaded rod attached to beam section 1 is taken into consideration. Thus, effective mass in Equation 2.22 is modified as

$$m_{eff} = \left(\frac{2I_0}{(t_3 + t_2)^2} + 2m_3 + 4m_1 + m_{ECD} \right) \tag{2.35}$$

With the given design parameters and m_{ECD} being 0.185 kg, effective mass (m_{eff} = 3.8 kg) and the equivalent stiffness (k_{eq} = 28.22 kN/m) of the structure including ECD is obtained to be used in the logarithmic decrement method in order

to calculate the damping constant of the ring magnet.

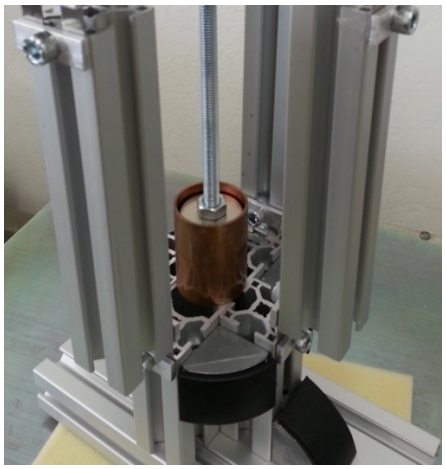

(a)

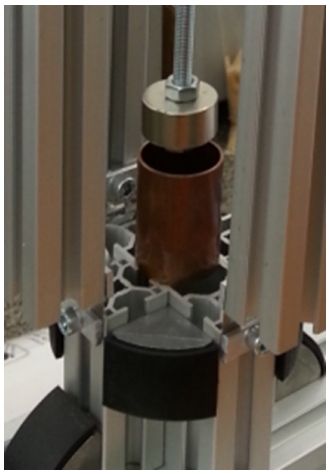

(b)

(c)

Figure 2.9. (a) Fully Inserted Ring Magnet. (b) Ring Magnet and Copper Tube Situated Separately. (c) Full View of the Four Legged Inertial Amplification Mechanism.

2.2.3.3. Laser Vibrometer Measurements to Estimate the ECD Constant. Logarithmic decrement method is used to obtain the damping constant ($c_{exp-logdec}$) of the ring magnet. The top surface speed of the inertial amplification mechanism setup is measured with a Laser Vibrometer when ECD effect is not included in the system. Afterwards, two consecutive measurements are taken when half of the ring magnet is within the copper tube and when it is fully inside the tube. The effect of ECD is seen in Figure 2.10. Note that the decay rate is highest when the ring magnet is fully inside the tube.

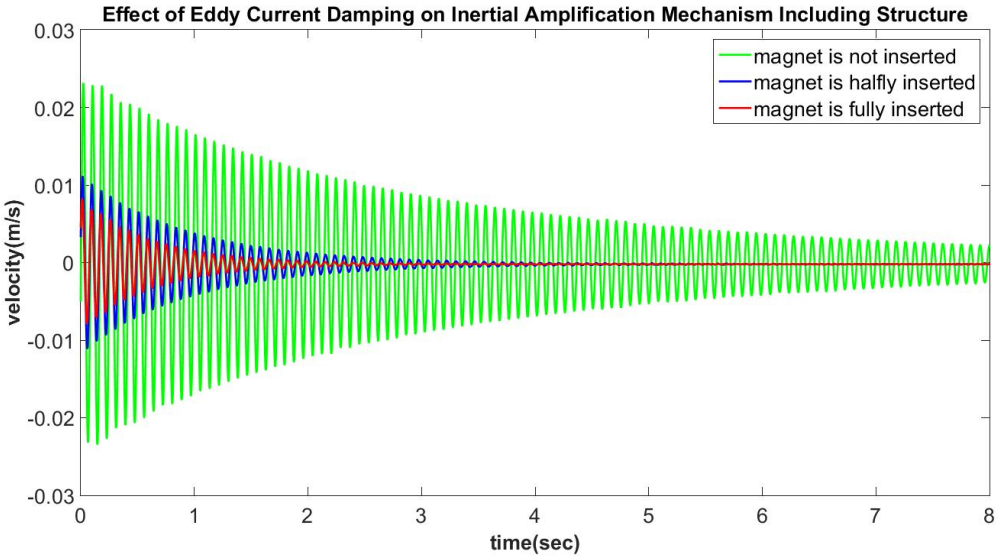

Figure 2.10. Laser Vibrometer Measurements of the Four Legged Inertial Amplification Mechanism.

Generally, this method can be formulated as follows [45]:

$$\delta = \frac{1}{n} ln \left(\frac{x(t)}{x(t+nT)} \right) \tag{2.36}$$

$$\zeta = \frac{\delta}{\sqrt{4\pi^2 + \delta^2}} \tag{2.37}$$

where δ is the logarithmic decrement, $x(t)$ is the peak displacement amplitude at time t, $x(t+nT)$ is the peak displacement amplitude after n periods (T).

Notice that in Equation 2.36 displacement amplitude information is used. However, vibration velocity is measured by the laser vibrometer. Therefore, Equation 2.36 needs to be modified. Since this equation is derived by assuming that the motion is underdamped, displacement amplitudes are related by Equation 2.38

$$x(t+nT) = e^{-\zeta\omega_n nT}x(t) \tag{2.38}$$

where ω_n is the undamped natural frequency of the system. When we take the time derivative of Equation 2.38 the following equation is obtained:

$$v(t+nT) = e^{-\zeta\omega_n nT}v(t) \tag{2.39}$$

where $v(t)$ is the velocity amplitude at time t, $v(t+nT)$ is the velocity amplitude after n periods (T). There is a phase difference between peak velocity and peak displacement values. Nevertheless, for all values of t, the following relationship holds:

$$x(t)/x(t+nT) = v(t)/v(t+nT) = e^{\zeta\omega_n nT} \tag{2.40}$$

Therefore, Equation 2.40 can be used for the peak values in the velocity measurements. As a result, Equation 2.36 can be reformulated as

$$\delta = \frac{1}{n} ln\left(\frac{v(t)}{v(t+nT)}\right) \tag{2.41}$$

Logarithmic decrement (δ) and damping ratio (ζ) values for the three conditions shown in Figure 2.10 are obtained by Equation 2.41 and Equation 2.37 and they are shown in Table 2.4. Damping constant values given in Table 2.4 are calculated by Equation 2.42 in which modified effective mass in Equation 2.35 and equivalent stiffness in Equation 2.15 are used.

$$c = 2\zeta\sqrt{m_{eff}k_{eq}} \tag{2.42}$$

Table 2.4. Calculated Damping Ratios and Constants According to Magnet Position via Logarithmic Decrement Method.

	No ECD		Half Inserted		Fully Inserted	
Peak Number	6th	33th	3rd	14th	3rd	22th
Time (s)	0.4354	2.658	0.1812	1.087	0.1771	1.74
Velocity (m/s)	2.04	0.9608	0.9301	0.3429	0.6319	0.03467
δ	0.028		0.091		0.153	
ζ	0.00446		0.0145		0.0243	
c (kg/s)	2.92		9.50		15.91	

When the damping constant for no eddy current damping case (just structural damping case) is subtracted from the fully inserted case $c_{exp-logdec}$ for the ring magnet is obtained as 12.99 kg/s. In Table 2.5 analytically, numerically and experimentally obtained damping constants are given. The difference seen in the analytically calculated ones with the others is due to the dipole approximation. It is seen that dipole approximation is not applicable for magnets having comparable height with respect to the inner radius of the copper tube.

Table 2.5. Analytical, Numerical and Experimental Damping Constant (kg/s) Estimations.

$c_{ana-dipole}$	$c_{ana-power}$	$c_{numerical}$	$c_{exp-freefall}$	$c_{exp-logdec}$
7.18	6.77	13.45	12.50	12.99

2.3. Finite Element Analysis

In order to see the frequency response of the four legged structure, a finite element model is built by using ANSYS-Workbench 14.5 as shown in Figure 2.11 (a). Point masses are added to the top and bottom portion to include the fasteners' masses. Since the structure is situated vertically, the bottom portion is assumed to be fixed during modal analysis.

Then the four legged structure is modified when the components of ECD mechanism including copper tube, threaded bolt and ring magnet are included into the design as shown in Figure 2.11 (b).

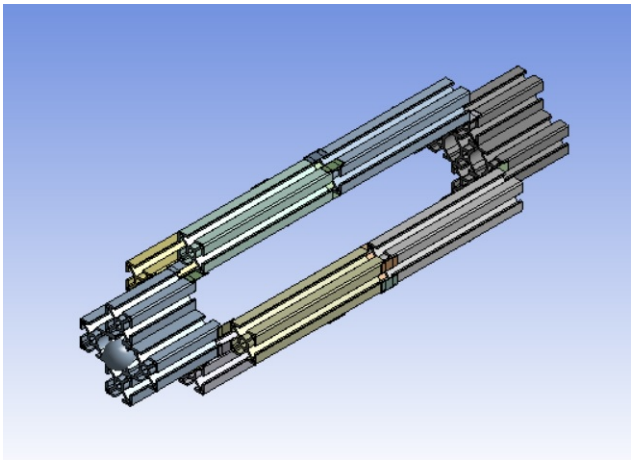

(a)

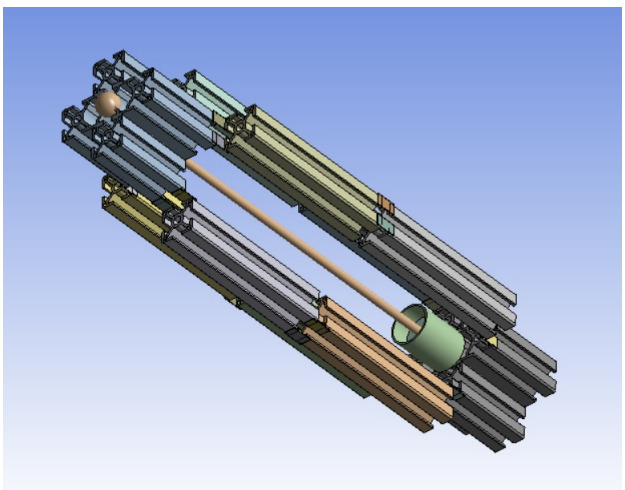

(b)

Figure 2.11. (a) Inertial Amplification Mechanism without ECD, (b) Inertial Amplification Mechanism with ECD.

2.3.1. Modal Analysis

Modal analysis for the structure w/ and w/o ECD mechanism is performed up to 700 Hz. The natural frequencies corresponding to each mode shape is found as given in Table 2.6. The first column shows the natural frequencies of the design given in Figure 2.11 (a). The second column shows the natural frequencies of the ECD

included structure given in Figure 2.11 (b).

Table 2.6. Undamped Natural Frequencies of the Four Legged Inertial Amplification Mechanism w/o and w/ ECD mass up to 700 Hz.

Mode Number	Nat. Freqs. w/o ECD mass (Hz)	Nat. Freqs. w/ ECD mass (Hz)
1	23.3	14.3
2	34.6	147.9
3	34.8	150.8
4	126.4	154.4
5	196.1	155.1
6	200.7	255.4
7	250.8	261.8
8	352.5	286.6
9	359.8	353.6
10	407.4	397.0
11	427.2	432.9
12	522.1	436.2
13	547.4	444.0
14	575.5	452.2
15	583.3	468.2
16	602.1	471.3
17	611.1	473.1
18	616.7	475.9
19	637.9	516.9
20	658.3	542.0
21	673.3	560.2
22	685.2	620.0
23	692.2	628.4
24	–	651.7
25	–	659.0

2.3.2. Harmonic Analysis

In order to include the ECD effect to the structure, a damping constant should be selected among the various estimations in Table 2.5. As the free fall experiment is widely used in the literature, $c_{exp-freefall} = 12.50$ kg/s is chosen to be used. Moreover, this value is also quite close to the other experimental and numerical estimations ($c_{exp-logdec} = 12.99$ kg/s and $c_{numerical} = 13.45$ kg/s). A damper with a damping constant of 12.50 kg/s is added to the structure as shown in Figure 2.12 in between the circumference of the top portion of copper tube and the lateral surface of the ring magnet.

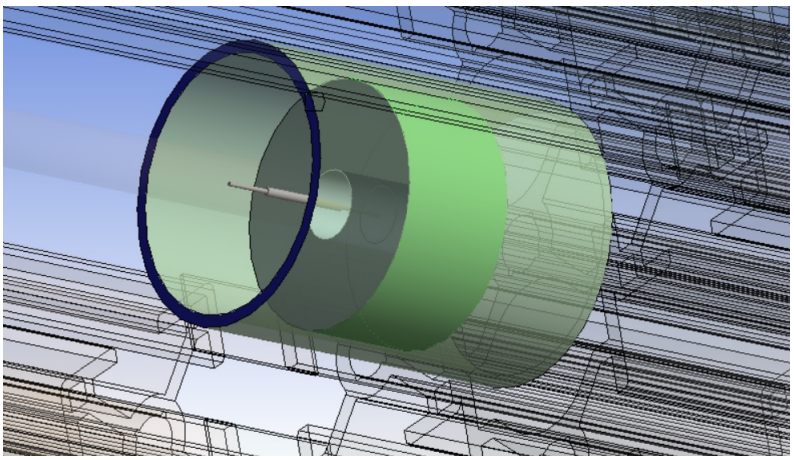

Figure 2.12. ECD Representation in the FEM.

During the harmonic analysis the damper shown in Figure 2.12 is initially not activated. Then, the damper is activated to see the changes in the resonance peaks. In Figure 2.13, frequency response results of two cases which are; four legged structure w/ ECD mechanism included when it is not activated and w/ ECD mechanism included when it is activated are shown. When ECD mechanism is activated it is seen that the first resonance peak is significantly suppressed without altering the other peaks. Besides, an almost resonance free frequency range is observed between 14.3 Hz and 516.9 Hz. The resonances in Table 2.5 are not observed much in this frequency range as the structure is forced axially.

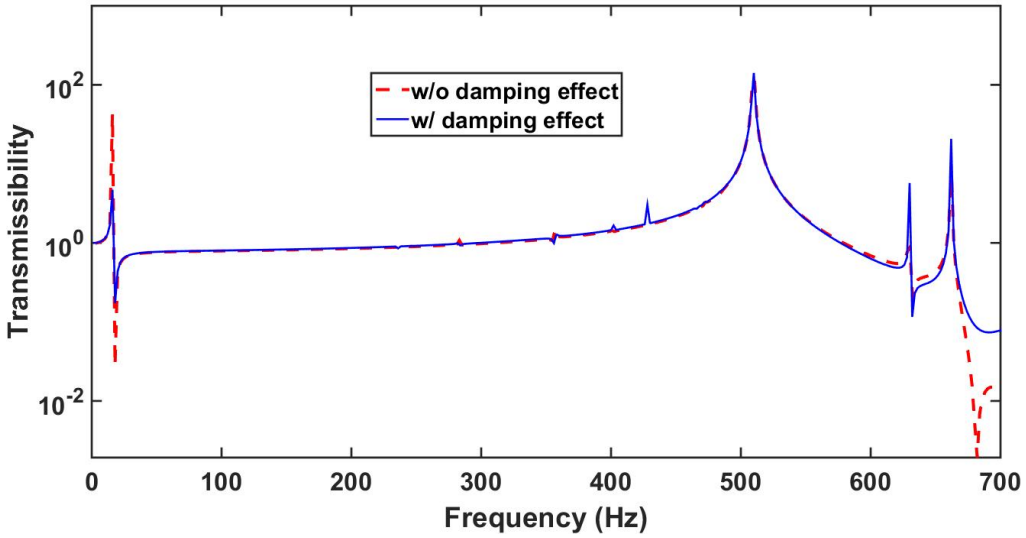

Figure 2.13. Frequency Response Results of the Four Legged Structure when the ECD Mechanism is Activated and not Activated.

3. LOCALLY RESONANT PERIODIC STRUCTURE

In this part of the research, ECD is combined with the local resonance method for the first time. A 1D periodic structure is designed that shows a wide local resonance induced band gap. The periodic structure is manufactured to see the effect of ECD on resonance peaks, stop band width, and anti-resonance depth in the frequency response plots.

ECD within the periodic structure are realized through ring magnet and copper tube assemblies. Electromagnetic FEMs of these assemblies are formed to calculate their damping coefficients. Moreover, structural FEMs of the periodic structure are generated to be used for modal analysis. The equivalent viscous damping coefficients of the ring magnet and copper tube assemblies are used in the structural finite element and lumped parameter models. Finally, frequency response results of the lumped parameter and FEMs are compared.

3.1. Analytical Model

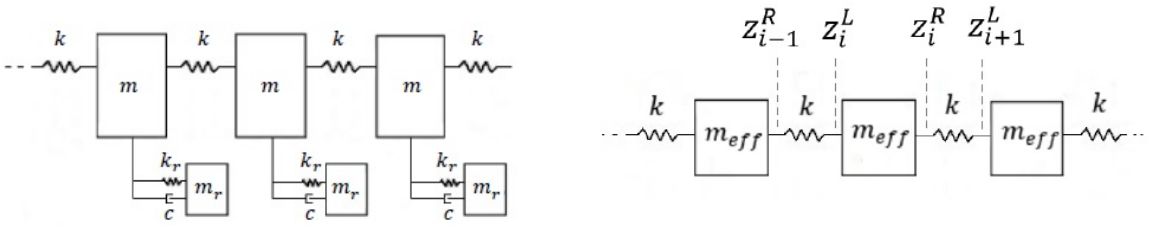

(a) (b)

Figure 3.1. Lumped Parameter Model of the Locally Resonant Periodic Structure Including ECD. (a) 1D Array with Local Resonators, (b) The Equivalent Array with Effective Mass.

A 1D locally resonant periodic structure that includes ECD is modelled as in Figure 3.1. During modeling of the periodic structure, five parameters are taken into

account, which are resonator mass (m_r), total mass of the remaining parts in the unit cell when the resonator mass is excluded (m), stiffness of the spring connecting the resonator mass to the unit cell (k_r), total stiffness between the unit cells (k) and the ECD constant (c). As ECD force is velocity proportional, c can be considered as a viscous damping constant.

Phononic band structure and the frequency response of the periodic structure will be determined by the transfer matrix method [46]. Through mechanical impedance to mass conversion, periodic structure's effective mass can be calculated to be used in its overall transfer matrix. Mechanical impedance representations for mass, spring and damper elements are $j\omega m$, $k/j\omega$ and c, respectively [47]. By using these impedances, effective mass of the unit cell of the system shown in Figure 3.1(b) is obtained as follows.

$$m_{eff} = m + \frac{1}{\frac{1}{m_r} - \frac{\omega^2}{k_r + j\omega c}} \tag{3.1}$$

The point transfer matrix for m_{eff} given in Equation 3.2 and the field transfer matrix for k given in Equation 3.3 are used [46] to obtain the relationship between the consecutive unit cells through the state vector relationships as shown in Equation 3.4.

$$P_i = \begin{bmatrix} 1 & 0 \\ -m_{eff}\omega^2 & 1 \end{bmatrix} \tag{3.2}$$

$$F_i = \begin{bmatrix} 1 & \frac{1}{k} \\ 0 & 1 \end{bmatrix} \tag{3.3}$$

$$\underline{z}_i^R = \begin{bmatrix} u \\ N \end{bmatrix}_i^R \tag{3.4}$$

where u is displacement and N is internal force. To construct the band structure of the locally resonant periodic structure including ECD, Bloch's Theorem given in Equation 3.5 is applied [48].

$$\underline{z}_i^R = \underline{z}_{i-1}^R e^{i\gamma} \tag{3.5}$$

Here, γ represents the wave number. Equations 3.4 and 3.5 can be used to obtain the relationship between the state vectors for the successive unit cells given in Equation 3.6.

$$\begin{bmatrix} u \\ N \end{bmatrix}_i^R = \begin{bmatrix} 1 & 0 \\ -m_{eff}\omega^2 & 1 \end{bmatrix} \begin{bmatrix} 1 & \frac{1}{k} \\ 0 & 1 \end{bmatrix} \begin{bmatrix} u \\ N \end{bmatrix}_i^R e^{-i\gamma} \tag{3.6}$$

Due to periodic boundary conditions, the determinant expressed in Equation 3.7 is obtained.

$$\begin{vmatrix} 1 - e^{i\gamma} & \frac{1}{k} \\ -m_{eff}\omega^2 & \frac{-m_{eff}\omega^2}{k} + 1 - e^{i\gamma} \end{vmatrix} = 0 \tag{3.7}$$

Consequently, dispersion equation given in Equation 3.8 for the periodic structure including infinite number of unit cells is attained. ω values that satisfy this dispersion equation are obtained for γ values in between 0 and π. As a result, the five aforementioned design parameters can be optimized for a desired band gap width.

$$1 - 2e^{i\gamma} + e^{2i\gamma} + \frac{m_{eff}\omega^2 e^{i\gamma}}{k} = 0 \tag{3.8}$$

On the other hand, to obtain the transmissibility plot for the periodic structure with a finite number of unit cells, overall transfer matrix of the structure should be

calculated by using Equations 3.2 and 3.3. In the overall transfer matrix, the U_{22} entry is used to find the displacement or acceleration transmissibility ($TR(\omega)$)(see Equation 3.10)

$$U_{overall} = (P_i F_i)^n = \begin{bmatrix} U_{11} & U_{12} \\ U_{21} & U_{22} \end{bmatrix} \quad n = 1, 2, 3, \ldots \tag{3.9}$$

$$TR(\omega) = \left| \frac{x(\omega)}{y(\omega)} \right| = \left| \frac{\ddot{x}(\omega)}{\ddot{y}(\omega)} \right| = \frac{1}{U_{22}} \tag{3.10}$$

where $x(\omega)$ and $y(\omega)$ are the output and input displacements. Moreover, the frequency range where $TR(\omega) < 1$ is defined as the stop band.

In order to show the effect of ECD on the frequency response of the periodic structure, its lumped parameter model is optimized to obtain a stop band between 50-100 Hz frequency range. During optimization, parametric studies are conducted with the use of the dispersion equation (Equation 3.8) and the transmissibility (Equation 3.10) of the lumped parameter model shown in Figure 3.1.

3.2. Parametric Studies

First two parametric studies focuses on the effect of mass distribution within the unit cell and the number of unit cells to the width and depth of the stop band of the periodic structure. While the latter two focuses on the effect of ECD to the frequency response of the periodic structure.

First of all, the effect of the main mass (m) to resonator mass (m_r) ratio is investigated. In this study, two different ring magnets with masses 0.032 kg and 0.052 kg are planned to be used for ECD purposes. Thus, the main mass (m) of the unit cell including these magnets is predicted to be around 0.1 kg. On the other hand, the resonator mass (m_r) which mainly consists of copper tube can be varied to change the

band gap frequency range. Figure 3.2 shows that as m/m_r ratio decreases, wider band gaps can be obtained. It is seen that $m/m_r = 1/3$ provides a band gap in the target frequency range $(50 - 100$ Hz). Moreover, $\sqrt{k_r/m_r}$ is taken as $2\pi \times 50$ so that, the lower limit of the stop band is around 50 Hz.

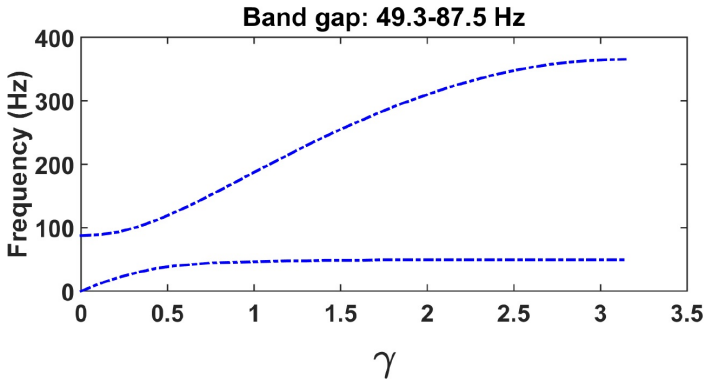

(a)

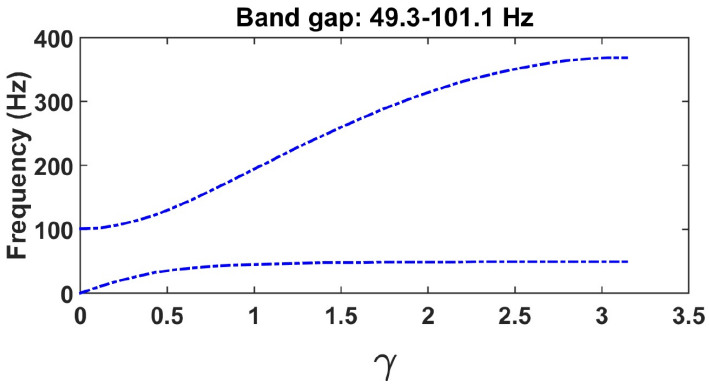

(b)

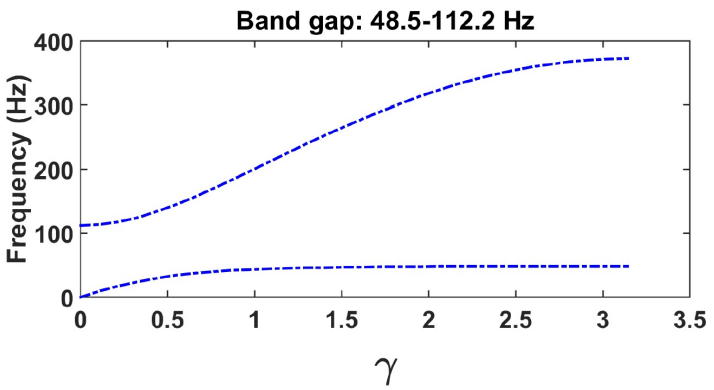

(c)

Figure 3.2. Band Structure Plots for Three Different Mass Ratios (a) $m/m_r = 1/2$, (b) $m/m_r = 1/3$, (c) $m/m_r = 1/4$. In all Plots $m = 0.1$ kg, $k = 126$ kN/m and $\sqrt{k_r/m_r} = 2\pi \times 50$ rad/s.

Secondly, the effect of number of unit cells to the width and depth of the stop band is investigated. Figure 3.3 shows that as the number of unit cells is increased, anti-resonance depth at 50 Hz also increases. Therefore, vibration isolation performance in between $50 - 100$ Hz is improved. However, as the number of unit cells increases, the overall size and mass of the periodic structure increases, as well. Considering the compromise between stop band depth and mass of the periodic structure, four unit cells are chosen to be used in the design.

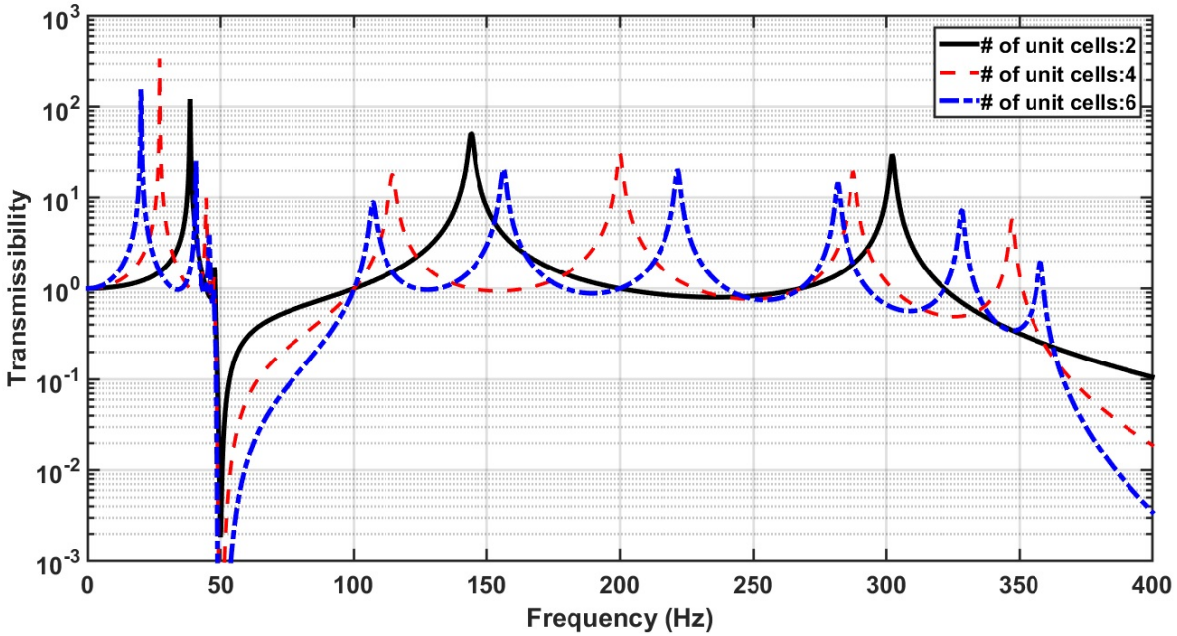

Figure 3.3. The Effect of Number of Unit Cells in the Periodic Structure on the Depth of the Stop Band between $50 - 100$ Hz. Here, $m = 0.1$ kg, $m_r = 0.3$ kg, $k = 126$ kN/m, $k_r = 29.6$ kN/m.

Within the unit cell of the periodic structure, a ring magnet will be used inside a copper tube to generate ECD. In the third parametric study, the effect of damping ratio to the stop band width and depth of the structure will be investigated. Only the ECD constant or equivalent viscous damping coefficient (c) will be varied in the lumped parameter model of the periodic structure. Figure 3.4 shows that as the damping ratio of the resonators (see Equation 3.11) increases all the resonance peaks and the

anti-resonance depth at 50 Hz decreases.

$$\zeta = \frac{c}{2\sqrt{m_r k_r}} \tag{3.11}$$

Also note that the increase in the damping ratio slightly increases the stop band width. However, if larger damping coefficients are to be realized by the use of larger magnets in the design, then the main mass m will increase. Consequently, m/m_r ratio will increase, resulting in a narrower stop band as shown in Figure 3.2(a).

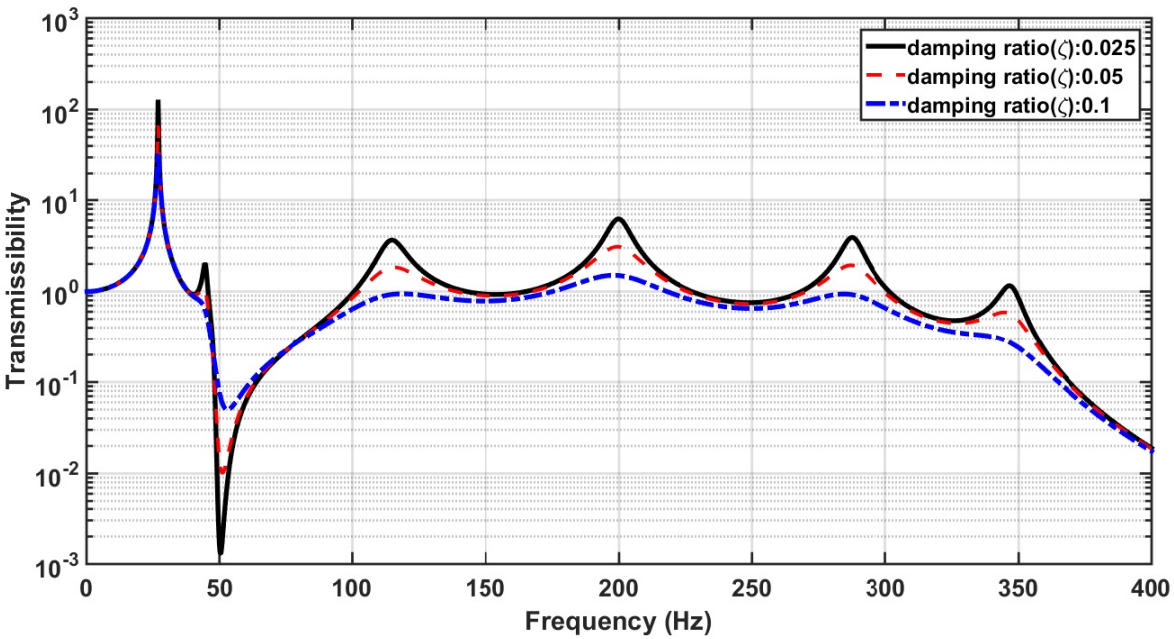

Figure 3.4. The Effect of Damping Ratio of the Resonators on Stop Band Width, Resonance Peaks and Anti-Resonance Depth for a Periodic Structure with Four Unit Cells. Here, $m = 0.1$ kg, $m_r = 0.3$ kg, $k = 126$ kN/m, $k_r = 29.6$ kN/m.

In the literature, many parametric studies are conducted regarding cylindrical magnets moving inside copper tubes. [34, 35, 40, 41, 44, 49] investigated the effect of cylindrical magnet's radius, height, and grade; copper tube's height and wall thickness, and the air gap width between this couple on the ECD force or Lorentz force. However, ring magnets are not investigated in these studies. [50] proposed a hybrid

damping structure including air damping and ECD. Yet, no parametric studies are done regarding the geometry of the ring magnet to be used.

Table 3.1. Dimensions, Weights and Remanent Flux Density Intervals of the Ring Magnets.

	Small Magnet	Large Magnet
Magnet Outer Radius (mm)	12.5	15.35
Magnet İnner Radius (mm)	4.25	4.25
Magnet Height (mm)	10	10
Magnet Weight (N)	0.31	0.51
Remanent Flux Density Interval (T)	$0.9 - 1.5$	$0.9 - 1.5$

Two set of NdFeB ring magnets (see Table 3.1) will be used in the locally resonant periodic structure to generate ECD. Notice that the remanent flux densities for these N35 grade magnets can be in a quite wide range depending on the manufacturer. In order to determine the remanent flux densities of these magnets accurately, free fall experiments are conducted. To that end, a 550 mm long 1.5 mm thick copper tube is used in which the ring magnets are let to free fall. The falling times for each ring magnet are measured with a digital chronometer. The average of 10 measurements are recorded. Later, the length of the copper tube is divided to these falling times and terminal velocities are obtained. Since at terminal velocity ($v_{terminal}$) Lorentz force ($F_{lorentz}$) is equal to the weight of the magnet (mg), by dividing the Lorentz force to the terminal velocity, damping constant (c) can be obtained as in Equation 3.12.

$$c = \frac{F_{lorentz}}{v_{terminal}} = \frac{mg}{v_{terminal}} \tag{3.12}$$

Following this experiment, an electromagnetic FEM which is a duplicate of this experiment is prepared. During the finite element analysis (FEA), remanent flux densities for each ring magnet are varied from 0.9 T to 1.5 T with 0.01 T increments to get the same terminal velocity values as in the free fall experiment. In Table 3.2,

corresponding remanent flux densities are given.

Table 3.2. Free Fall Experiment Results for Ring Magnets. Here, the Copper Tube is 550 mm Long, 1.5 mm Thick and It's Inner Diameter is 32 mm.

	Small Magnet	Large Magnet
Measured Falling Time (s)	3.18	9.59
Terminal Velocity (m/s)	0.173	0.057
Lorentz Force (N)	0.31	0.51
Damping Constant (kg/s)	1.81	8.90
Remanent Flux Density (T)	1.03	1.14

A final parametric study will be conducted to obtain the maximum amount of damping for the given ring magnets. To that end, an electromagnetic FEM of the ring magnets and copper tube will be generated. The magnets will be subjected to free fall due to gravity and the Lorentz force between magnets and copper tubes will be calculated. During the analyses, mass of the copper tube is kept constant at 0.3 kg. Moreover, its inner radius is fixed at 16 mm while its height and wall thickness is varied considering the mass constraint. Height of the tube is decreased as the wall thickness is increased from 1 mm to 20 mm with 1 mm increments.

One of these analyses is shown in Figure 3.5. Here, the wall thickness of the copper (ρ = 8700 kg/m^3) tube is 11 mm, and its height is 23.2 mm satisfying the mass constraint of 0.3 kg. Notice that as the magnet velocity reaches a terminal value, the Lorentz force in the direction of free fall (z-direction) reaches 0.51 N, which is the weight of the large magnet. Then, damping constant can be found using Equation 3.12. For this case, $v_{terminal} = 0.0167$ m/s giving $c = 30.5$ N.s/m.

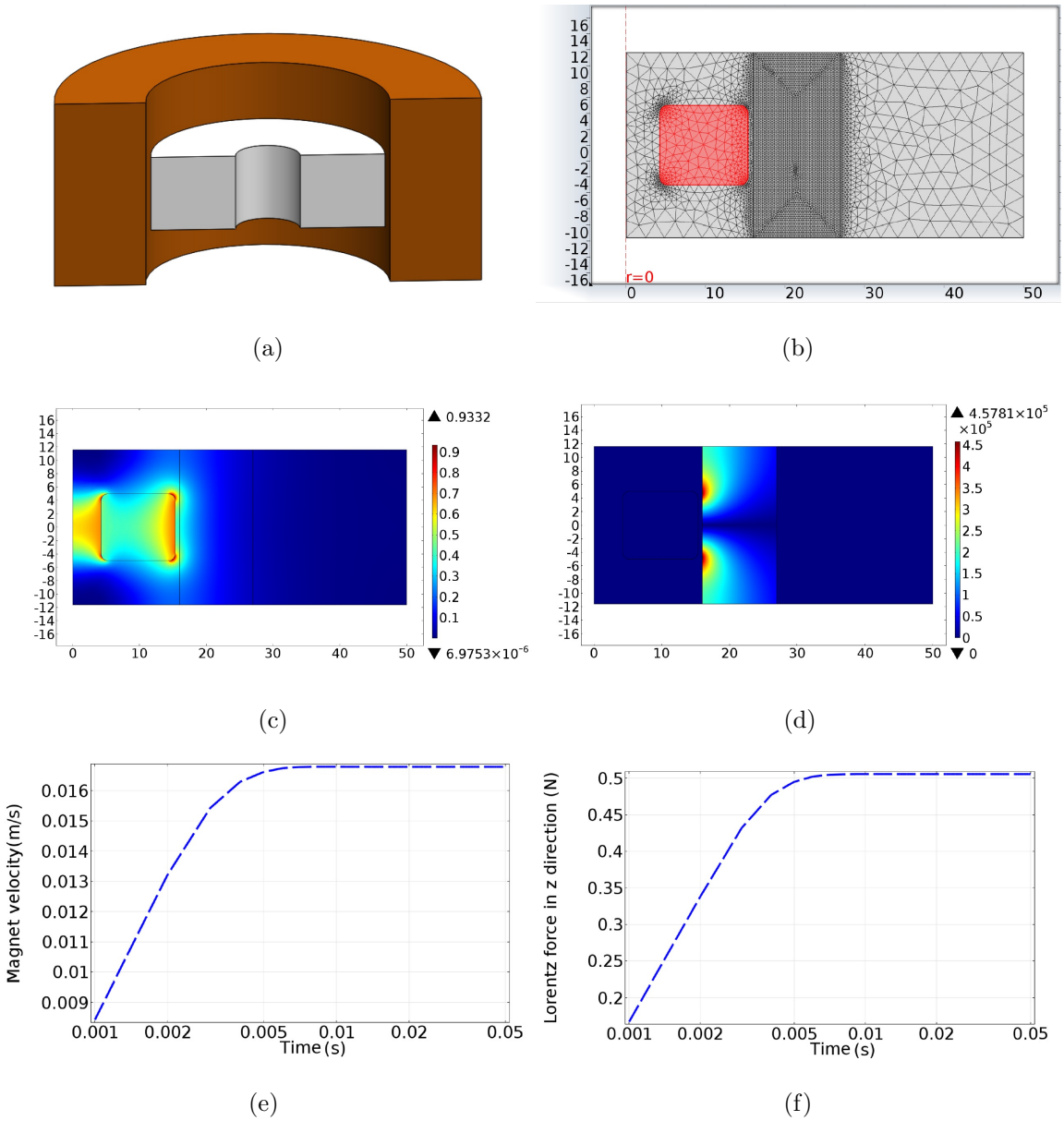

Figure 3.5. Computational Analysis for the Free Fall of the Large Ring Magnet Inside a Copper Tube with 11 mm Wall Thickness and 23.2 mm Height. (a) Section View, (b) 2D Axi-Symmetric Meshed Geometry, (c) Magnetic Density Norm (T) Contour Plot, (d) Current Density Norm (A/m^2) Contour Plot, (e) Relative Velocity Between Magnet and Copper Tube, (f) Lorentz Force Between Magnet and Copper Tube that is Generated due to Eddy Currents within the Copper Tube.

Figure 3.6 shows the effect of wall thickness of the copper tube on the ECD constant and the damping ratio of the resonator. It is seen that to acquire the maximum damping ratio with a mass constraint, there is an optimum copper wall thickness value.

For a copper tube having an inner radius of 16 mm with mass constraint of 0.3 kg, the optimum wall thickness value is around 11 mm.

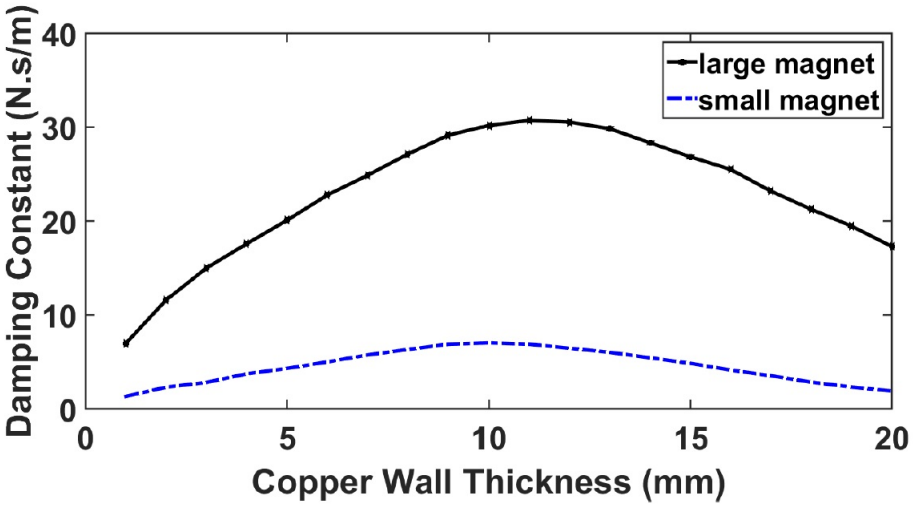

(a)

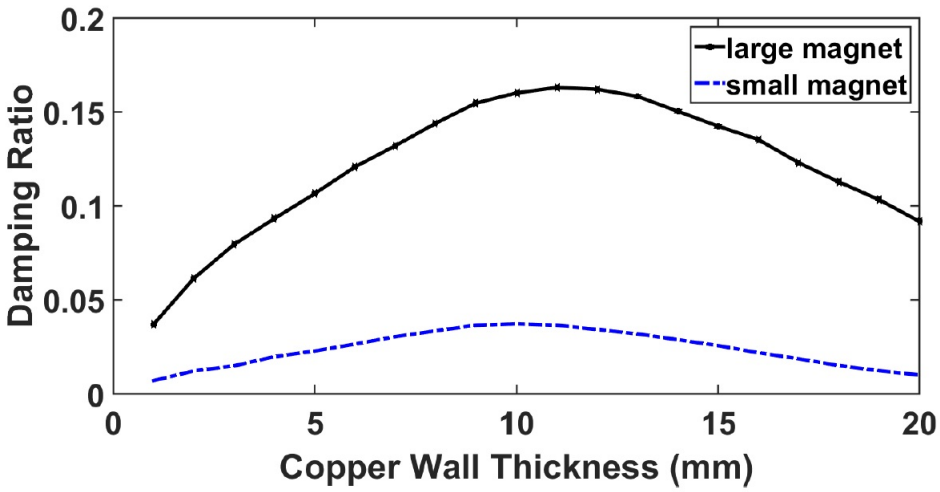

(b)

Figure 3.6. The Effect of Copper Tube's Wall Thickness on Damping Behaviour for a Constant Resonator Mass of 0.3kg (a) Effect of the Copper Wall Thickness on Damping Constant, (b) Effect of Copper Tube Wall Thickness on Damping Ratio. Here, $m_r = 0.3$ kg, $k_r = 29.6$ kN/m.

3.3. Design and Finite Element Analysis

In Figure 3.7, lumped parameter model of the unit cell of the periodic structure and the corresponding distributed parameter model can be seen. In Figure 3.7(b) two sets of parallel spiral springs are used to realize the stiffnesses k and k_r. The two parallel spiral springs ($k_r/2$) that are attached to the copper tube (m_r) allow the ring magnet to move concentrically inside the tube without any contact. Notice that as the large magnet diameter is 30.7 mm and the inner diameter of the tube is 32 mm, there is very little clearance between them. The other two parallel spiral springs ($k/2$) are used to connect the unit cells with each other. Due to their parallel design, they only allow axial relative motion between the unit cells. As a result, 1D locally resonant periodic structure can be realized.

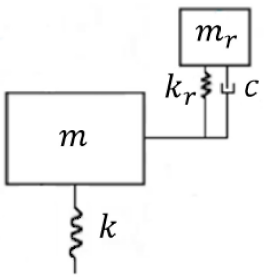

(a)

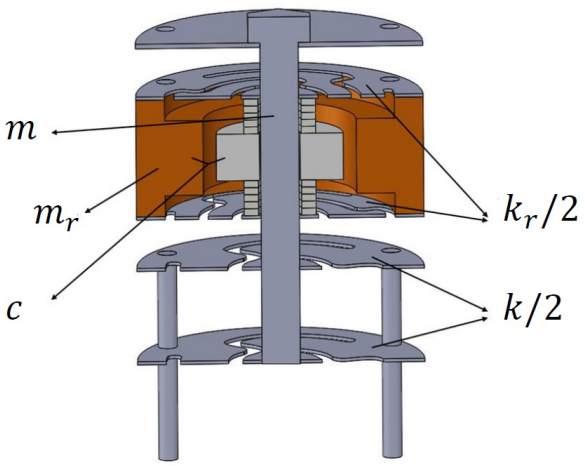

(b)

Figure 3.7. (a) Lumped Parameter Model of the Unit Cell. (b) Distributed Parameter Model of the Unit Cell.

In the analyses with the lumped parameter model, the stiffnesses k_r and k are determined as 29.6 kN/m and 126 kN/m (see Figures 3.3 and 3.4). In order to realize these stiffness values, the spiral springs shown in Figure 3.8(a) and 3.8(b) are designed. Both of these stainless steel ($E = 193$ GPa, $\rho = 7750$ kg/m^3, $\nu = 0.31$) springs have 60 mm outer diameter, 8.5 mm inner diameter and 0.7 mm thickness. The spiral shaped slots are chosen such that the stiffness of these springs are close to half of the stiffness values in the lumped parameter model.

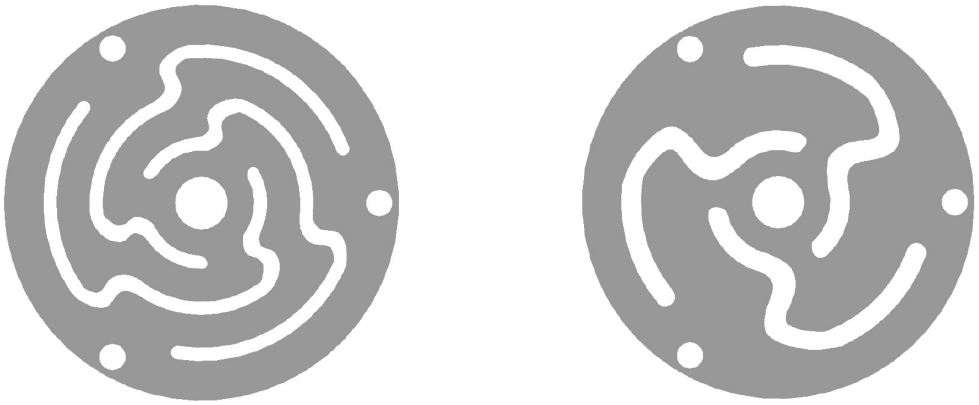

(a) (b)

Figure 3.8. (a) Spiral Spring with $k_r/2 = 13.5$ kN/m Stiffness. (b) Spiral Spring with $k/2 = 62.0$ kN/m Stiffness

The locally resonant periodic structure with four unit cells can be seen in Figure 3.9. The whole structure has an outer diameter of 60 mm and length of 376 mm. Notice that the central stainless steel M8 bolts connect all parts within each unit cell. The bolt head is connected to a stainless steel circular plate that has 1 mm thickness. Moreover, three stainless steel M4 bolts are used near the periphery of each circular plate to make the connection with the neighbouring unit cell. Small plastic rings and nuts with negligible masses will be used during the assembly of the locally resonant periodic structure. However, as the effect of these plastic parts are assumed to be negligible, they are not included in the model shown in Figure 3.9.

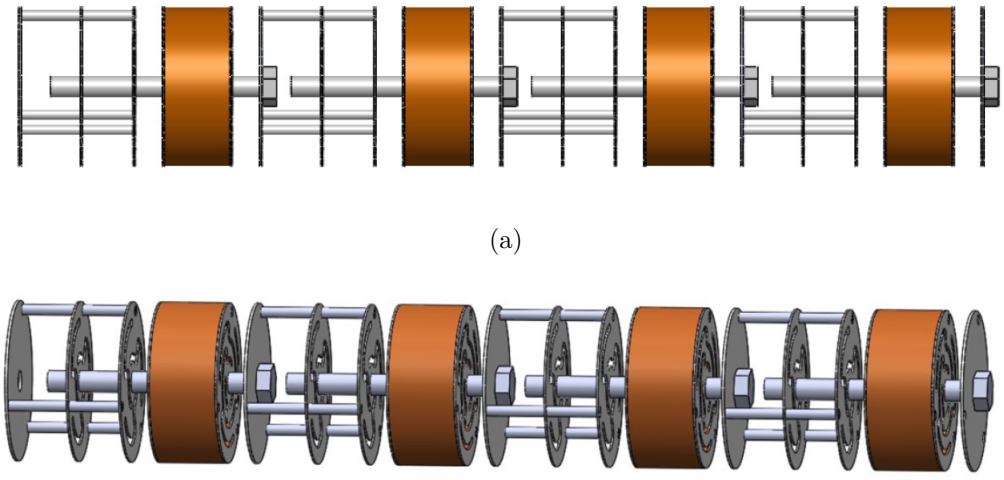

(a)

(b)

Figure 3.9. The Locally Resonant Periodic Structure with Four Unit Cells. (a) Isometric View and (b) Side View.

In the parametric studies with the lumped parameter model, m and m_r were taken as round numbers like 100 gr and 300 gr. When the distributed parameter model of the structure is formed, m is calculated as 0.143 kg for the unit cell with small magnet. However, m_r is 0.392 kg giving $m/m_r = 0.365$ which is close to the target mass ratio of 1/3. Furthermore, m becomes 0.162 kg and 0.111 kg for the unit cell with large magnet and no magnet. As a result, mass ratio for the large magnet and no magnet cases are 0.413 and 0.283, respectively.

The copper tube with mass m_r in Figure 3.7(b) does not have constant wall thickness as in Figure 3.5(a). Notice that the wall thickness is smaller on the two faces allowing room for out-of-plane deformations of the spiral springs ($k_r/2$). The wall thickness in the middle cross-section is chosen as 14 mm, which is a little higher than the optimum value of 11 mm to compensate the decrease in the wall thickness on the two faces.

In Figure 3.10, electromagnetic FEA of the designed copper tube shape can be seen. Here, the large magnet is shown inside the tube. The same analysis is conducted for the small magnet, as well. As a result of these analyses, the damping constants

for the small and large magnets are found as 4.02 N.s/m and 20.4 N.s/m, respectively. These values are a little lower than the peak values in Figure 3.6(a). When the current density plots in Figure 3.5(d) and Figure 3.10(d) are compared, higher current densities are seen over larger areas in Figure 3.5(d). This explains the lower damping constants for the designed copper tube.

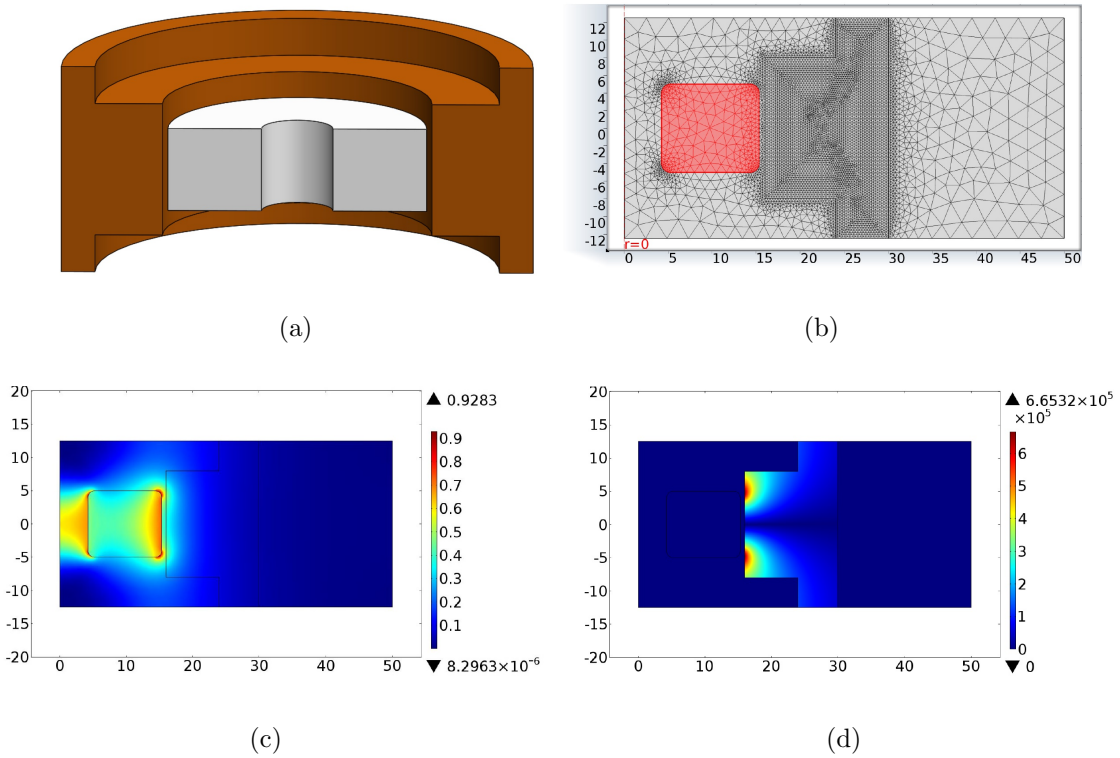

Figure 3.10. (a) Section View of a Large Ring Magnet Inside the Designed Copper Tube. (b) 2D Axi-Symmetric FEM of the Designed Copper Tube and Large Ring Magnet. (c) Magnetic Flux Density Norm (T) Contour Plot. (d) Current Density Norm (A/m^2) Contour Plot.

In order to check the effect of other elements within the resonator on the damping behaviour, a more detailed model of the resonator is analyzed. In Figure 3.11, the stainless steel ($\sigma = 1.32 \times 10^6$ Siemens/m) spiral springs $k_r/2$, stainless steel M8 bolt in the middle and the plastic rings that are used to separate the magnet and the spiral springs are included in the model.

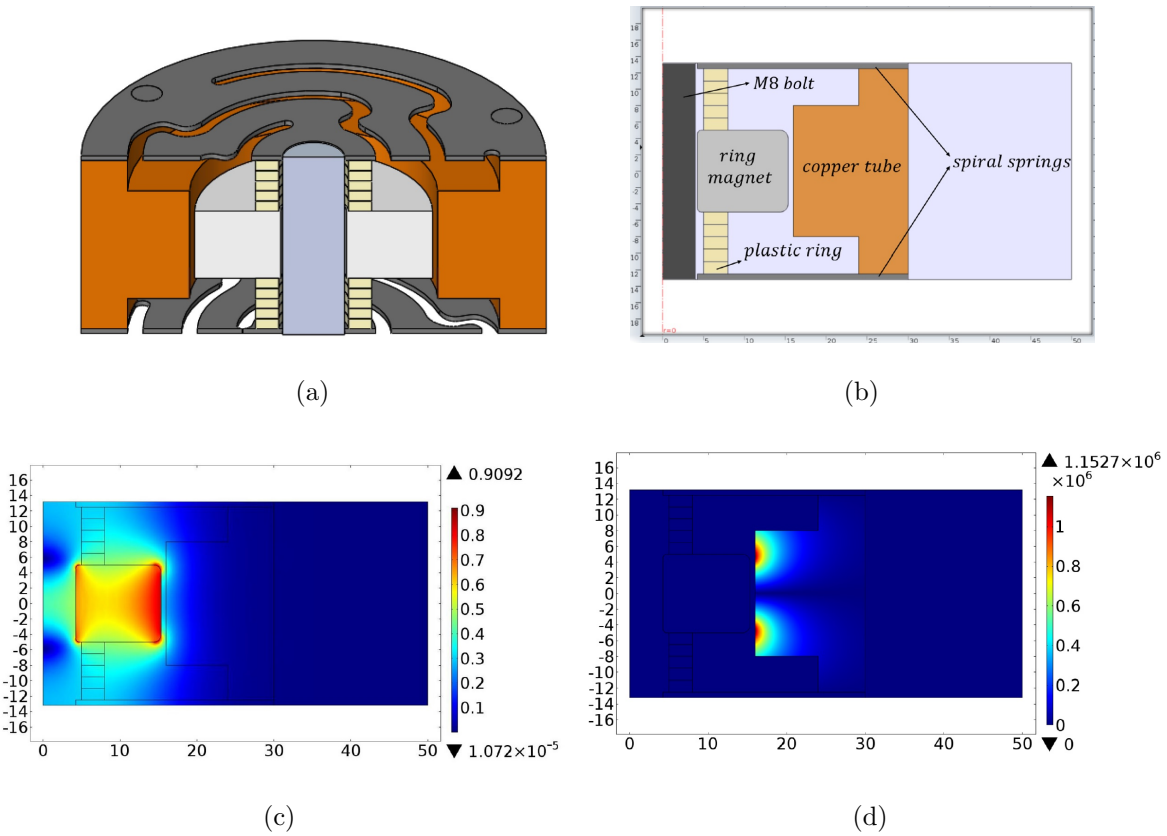

Figure 3.11. (a) Section View of the Fully Represented Resonator. (b) Fully Represented 2D Axi-Symmetric Resonator Geometry With Large Magnet Included. (c) Magnetic Flux Density Norm (T) Contour Plot. (d) Current Density Norm (A/m^2) Contour Plot.

As a result of this analysis, the damping constants for the small and large magnets are found as 2.31 N.s/m and 10.8 N.s/m, respectively. The smaller damping constant values in this analysis can be explained by observing that the stainless steel bolt and stainless steel spiral springs reduce magnetic flux density close to the copper tube (please compare Figures 3.10(c) and 3.11(c)). Consequently, smaller eddy current densities are obtained in Figure 3.11(d) when compared to Figure 3.10(d).

3.3.1. Structural Finite Element Analysis

The FEM of the locally resonant periodic structure shown in Figure 3.9 is formed and its first 10 natural frequencies are determined for three cases: resonators with no magnets, resonators with small magnets, and resonators with large magnets. The finite

element mesh for the case with small magnets can be seen in Figure 3.12. Similar mesh sizes are used in the other two cases. In all cases, the structures are fixed from the right side and frictionless supports are used around the resonators.

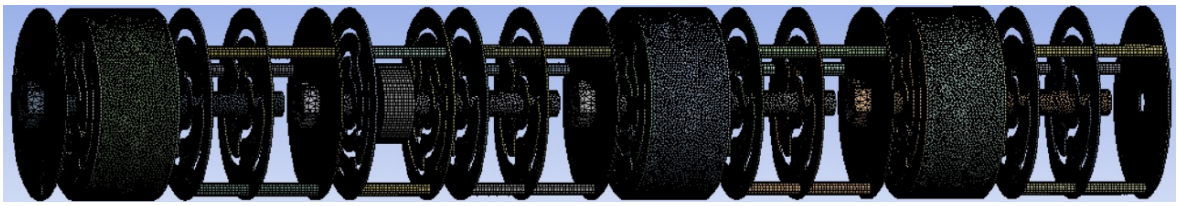

Figure 3.12. Finite Element Mesh for the Locally Resonant Periodic Structure with Small Magnets Included. The Resonator of the Second Unit Cell is Suppressed for Visual Purposes.

Table 3.3 shows the first 10 natural frequencies of the locally resonant periodic structure without any magnets. When the corresponding mode shapes are investigated, it is seen that the 5th mode is torsional as shown in Figure 3.13(b). Therefore, this mode is not expected to be seen in the frequency response if the system is excited axially. As a result, the stop band will occur between the 4th and 6th modes, which are shown in Figures 3.13(a) and 3.13(c).

Table 3.3. First 10 Natural Frequencies of the Periodic Structure without any Magnets. In the Last Row, Types of the Modes are Indicated as Axial (A) or Torsional (T).

Mode #	1	2	3	4	5	6	7	8	9	10
Freq. (Hz)	30.7	45.2	47.2	47.7	66.2	130.8	170.5	231.5	257.6	258.3
Mode Type	A	A	A	A	T	A	T	T	A	T

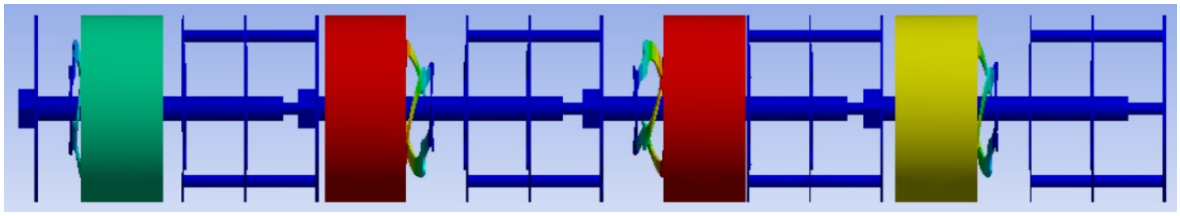

(a)

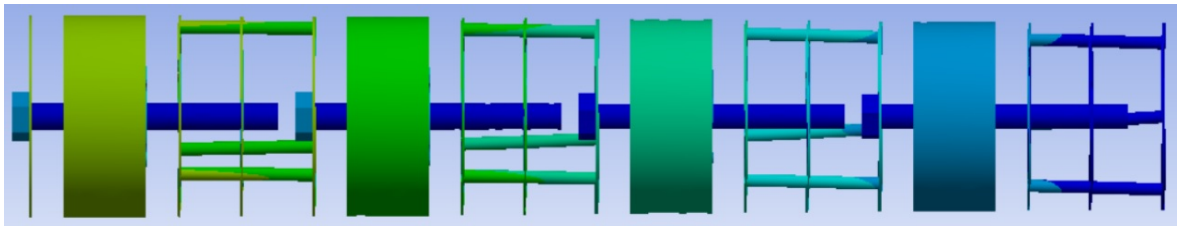

(b)

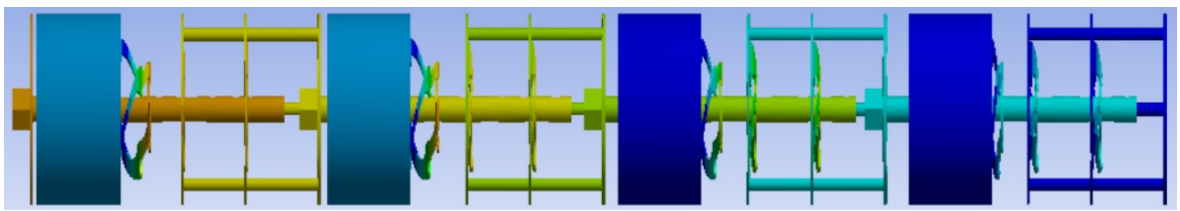

(c)

Figure 3.13. Mode Shapes of Periodic Structure without any Ring Magnets that Determine the Lower and Upper Limits of the Stop Band With a Torsional Mode in between. (a) 4th Mode Shape at 47.7 Hz, (b) 5th Mode Shape at 66.2 Hz and (c) 6th Mode Shape at 130.8 Hz.

Second modal analysis is done when small ring magnets are inserted inside the copper tubes. The first 10 natural frequencies are shown in Table 3.4. The stop band will occur in between 4th and 6th modes and they are depicted in Figure 3.14 with the torsional mode in between at 62.9 Hz. These limiting mode shapes are shown in Figures 3.14(a) and 3.14(c).

Table 3.4. First 10 Natural Frequencies of the Periodic Structure Including Small Ring Magnets. In the Last Row, Types of the Modes are Indicated as Axial (A) or Torsional (T).

Mode #	1	2	3	4	5	6	7	8	9	10
Freq. (Hz)	28.7	43.1	44.6	46.5	62.9	111.3	163.2	215.4	220.1	244.3
Mode Type	A	A	A	A	T	A	T	T	A	T

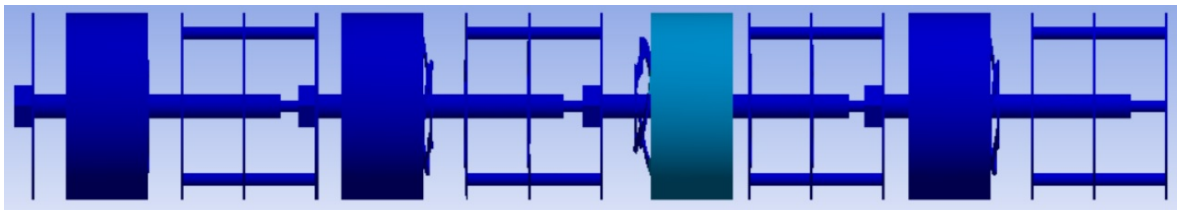

(a)

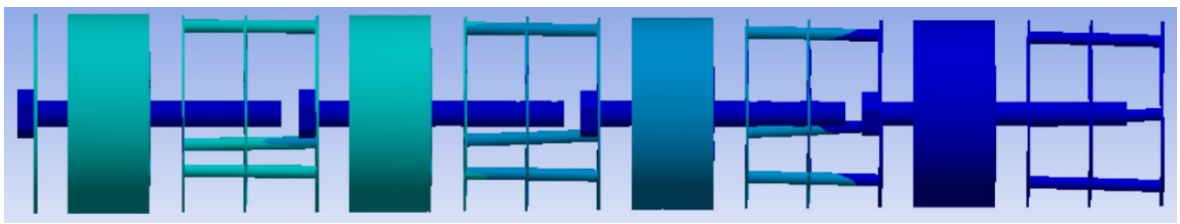

(b)

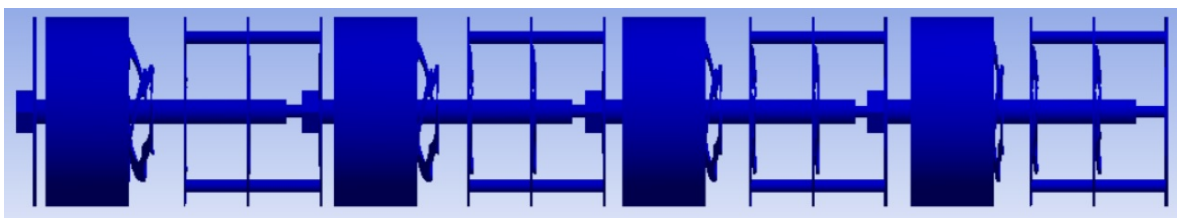

(c)

Figure 3.14. Mode Shapes of Periodic Structure with Small Magnets that Determine the Lower and Upper Limits of the Stop Band with a Torsional Mode in between. (a) 4th Mode Shape at 46.5 Hz, (b) 5th Mode Shape at 62.9 Hz and (c) 6th Mode Shape at 111.3 Hz.

Finally, a modal analysis is done when large ring magnets are inserted inside the copper tubes. The first 10 natural frequencies are shown in Table 3.5. The stop band

will again occur in between 4th and 6th modes with a torsional mode in between and they are shown in Figure 3.15.

Table 3.5. First 10 Natural Frequencies of the Periodic Structure Including Large Magnets. In the Last Row, Types of the Modes are Indicated as Axial (A) or Torsional (T).

Mode #	1	2	3	4	5	6	7	8	9	10
Freq. (Hz)	28.9	43.0	45.1	46.7	64.5	106.1	164.3	202.5	221.8	245.5
Mode Type	A	A	A	A	T	A	T	T	A	T

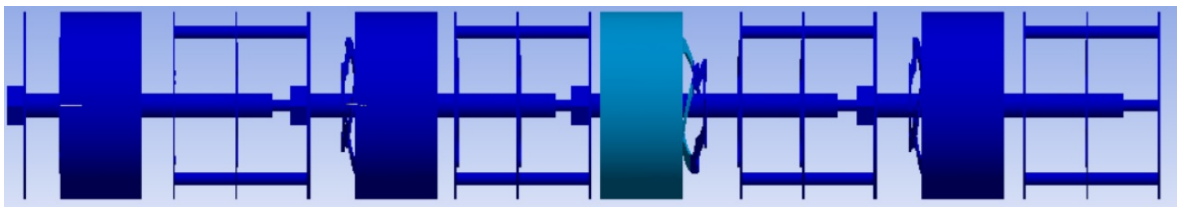

(a)

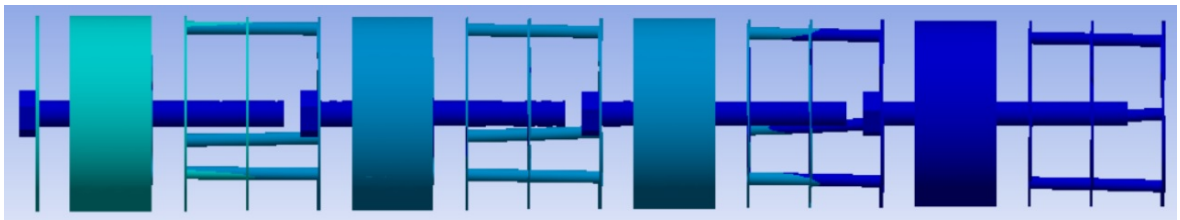

(b)

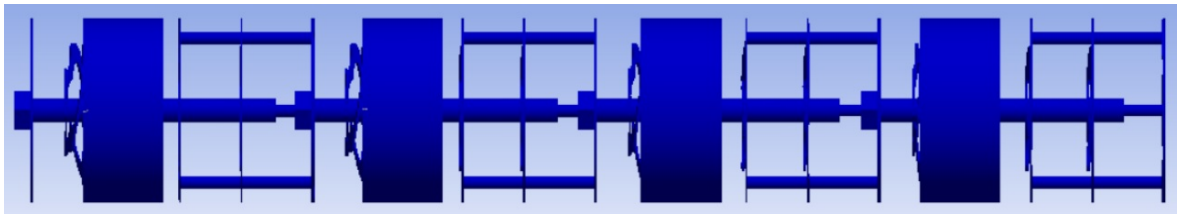

(c)

Figure 3.15. Mode Shapes of Periodic Structure with Large Magnets that Determine the Lower and Upper Limits of the Stop Band with a Torsional Mode in between. (a) 4th Mode Shape at 46.7 Hz, (b) 5th Mode Shape at 64.5 Hz and (c) 6th Mode Shape at 106.1 Hz.

3.4. Experimental Measurements and Results

3.4.1. Laser Vibrometer Measurements to Estimate the ECD Constants

To validate the damping constant values obtained through the electromagnetic FEA, measurements are taken via a laser vibrometer for the three types of resonators. Figure 3.16 shows one of these resonators.

Figure 3.16. Measured Resonator with Small Ring Magnet Inside.

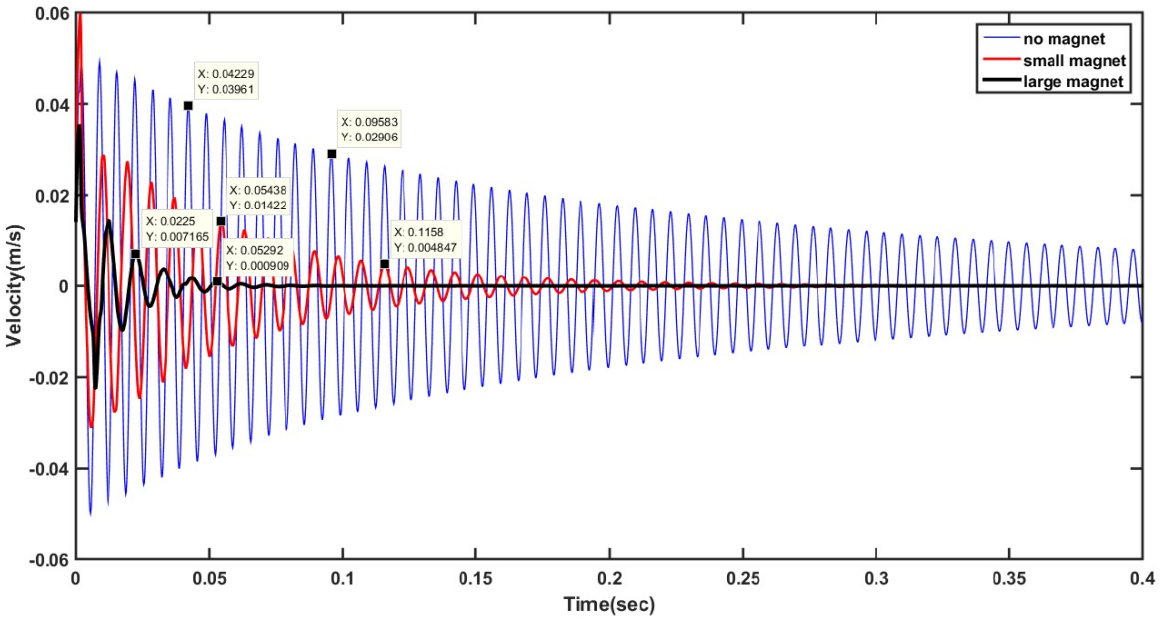

Figure 3.17. ECD Effect Measured with Laser Vibrometer.

In the first measurement no ring magnet is inserted inside the copper tube. In the second and third measurements, small and large ring magnets are inserted inside the copper tube to create ECD. The damping coefficient in all three case are calculated through Equation 3.13.

$$c = 2\zeta\sqrt{m_{eff}k_r} \tag{3.13}$$

In the experiments, the copper tube is fixed and the inner part is allowed to vibrate. Thus, effective mass (m_{eff}) used in Equation 3.13 differs depending on the mass of the magnet used inside the resonator (see Table 3.1). In Equation (3.13), $k_r = 27$ kN/m and ζ is determined by the logarithmic decrement method. Three different measurement results are shown in Figure 3.17 with six data points taken in order to apply the logarithmic decrement method via Equations 2.41 and 2.37.

In Table 3.6, peak points taken for each measurement to be used in logarithmic decrement method are given, which are followed by the calculated damping ratios and damping constants.

Table 3.6. Calculated Damping Ratios and Constants via Logarithmic Decrement Method.

	No Magnet		Small Magnet		Large Magnet	
Peak Number	7th	15th	7th	14th	3rd	6th
Time (s)	0.0423	0.0958	0.0544	0.1158	0.0225	0.0529
Velocity (m/s)	0.0396	0.0291	0.0142	0.00485	0.00716	0.000909
δ	0.0387		0.1537		0.6882	
ζ	0.0062		0.0245		0.1088	
m_{eff} (kg)	0.034		0.066		0.085	
k_r (kN/m)	27.0		27.0		27.0	
c (kg/s)	0.37		2.06		10.43	

If the damping constant of the no ring magnet case is subtracted from the other cases, ECD constants for each ring magnet can be obtained. Notice that these damping constant values are close to the values obtained through the fully represented resonator model (Figure 3.11).

3.4.2. Experimental Modal Analysis of the Prototype Produced

The prototype of the locally resonant periodic structure and the experimental setup can be seen in Figure 3.18. Notice that the prototype is hanged by rubber cords to simulate free boundary conditions. Excitation is given from one end by a modal shaker. The input acceleration is measured through an impedance head and the output acceleration on the other end of the prototype is measured by an accelerometer. Transmissibility is calculated as the ratio of output acceleration to input acceleration (see Equation 3.10).

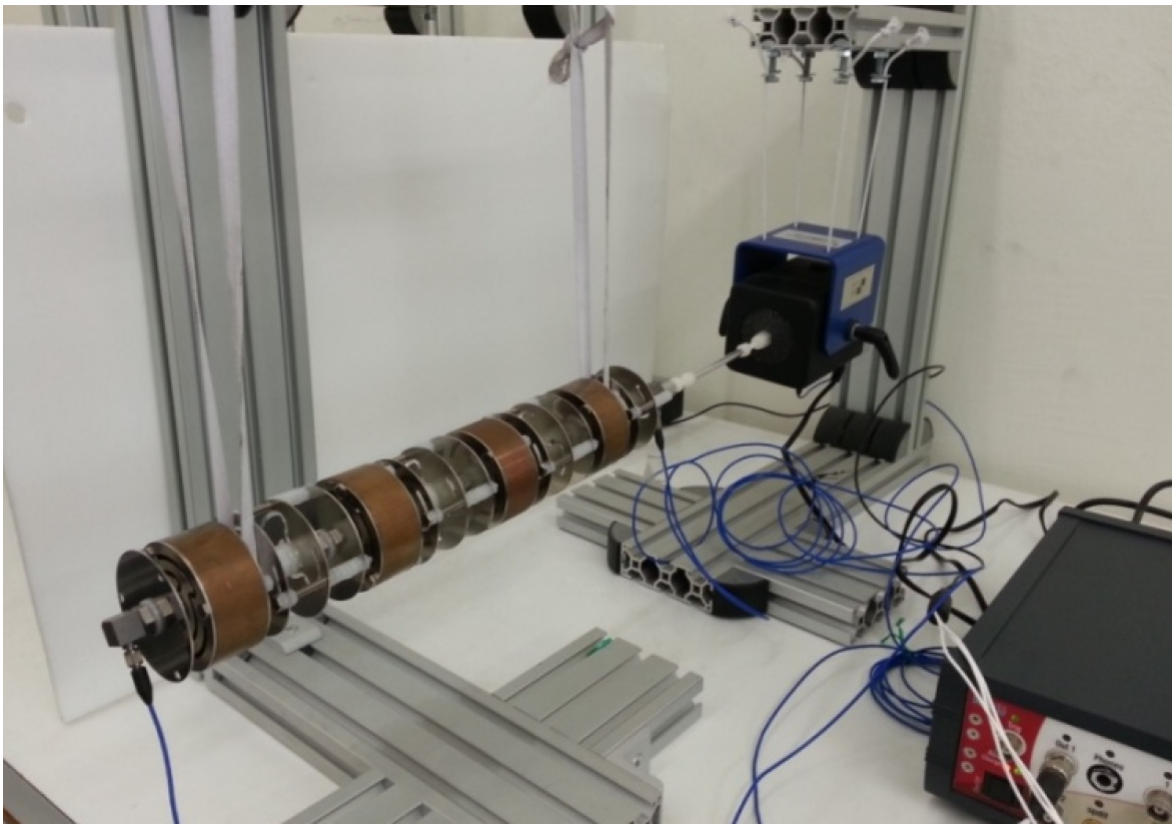

Figure 3.18. Experimental Setup for the Locally Resonant Structure.

In the three measurements taken, modal shaker excites the structure up to 400 Hz. In the first measurement, to observe the effect of structural damping effect within the prototype on the vibration stop band, ring magnets are not inserted inside the copper tubes. During the second and third measurements, small and large ring magnet are used, respectively. The effect of ECD can be seen in Figure 3.19 via the decrease in all resonance peaks. The stop band width does not change much due to magnet usage.

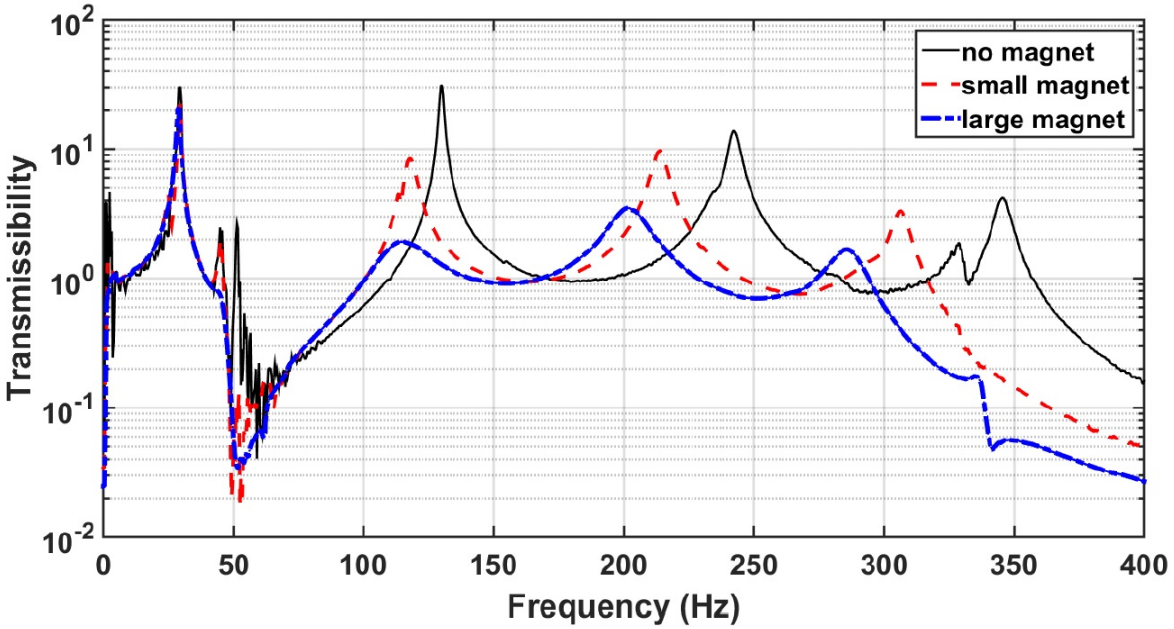

Figure 3.19. Frequency Response Results Obtained from the Experimental Measurements.

For comparison purposes, frequency response plots are obtained analytically and numerically using the lumped parameter and FEMs, respectively. In Figure 3.20, frequency response plots for the lumped parameter models can be seen. From the analytical calculations done by using the lumped parameter model without ring magnets, stop band is obtained in between $40.1 - 88.8$ Hz for $m_r = 0.392$ kg, $m = 0.111$ kg, $k = 124$ kN/m and $k_r = 27$ kN/m. When small ring magnets are included, stop band is obtained in between $38.7 - 80.9$ Hz for $m_r = 0.392$ kg, $m = 0.143$ kg, $k = 124$ kN/m and $k_r = 27$ kN/m. It is seen that only the m value changes due to small ring magnet inclusion. This causes a decrease in stop band width due to mass ratio (m/m_r) increase. Finally, when the large ring magnets are inserted inside the copper

tubes, stop band is obtained in between $37.4 - 78.8$ Hz for $m_r = 0.392$ kg, $m = 0.162$ kg, $k = 124$ kN/m and $k_r = 27$ kN/m. Inclusion of large ring magnets with higher damping decreases the stop band width. On the other hand, the resonance peaks are suppressed the most with the use of large ring magnets. Hence, there is a compromise between stop band width and damping.

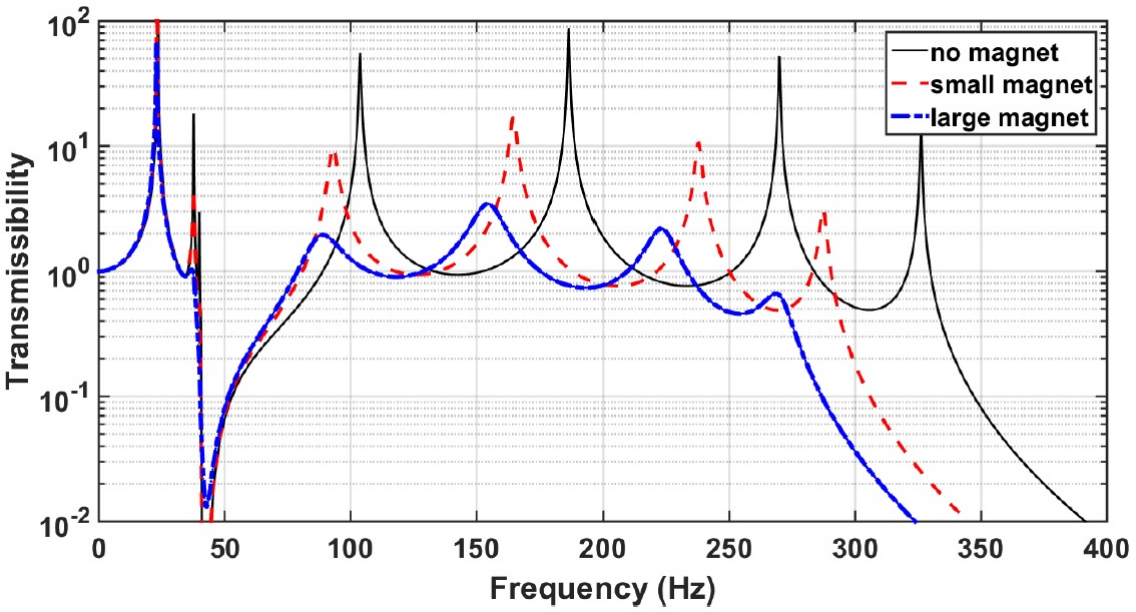

Figure 3.20. Frequency Response Results Obtained via the Lumped Parameter Models.

Figure 3.21 shows the frequency response plots for the FEMs. Notice that the frequency response plots obtained analytically, numerically and experimentally are quite similar (see Figures 3.19−3.21). There are small peaks around 60 Hz and 160 Hz in the numerical frequency response plot due to the torsional modes (see Tables 3.3−3.5). However, these peaks are insignificant and do not change the stop band characteristics. In Table 3.7, lower and upper stop band limits, and their ratios are presented. One can see that there are some shifts in the stop band frequency limits obtained through three different approaches. Nevertheless, ω_u/ω_l ratios are almost the same.

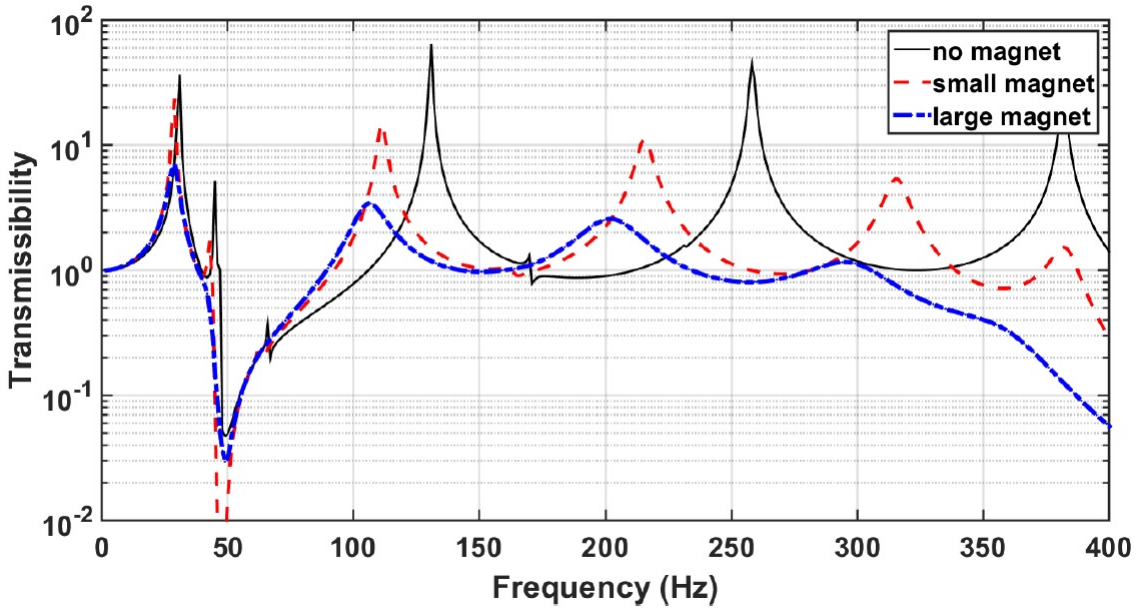

Figure 3.21. Frequency Response Results obtained via the FEMs.

Table 3.7. Lower (ω_l) and Upper (ω_u) Stop Band Limits, and Their Ratios (ω_u/ω_l) Obtained from the Analytical, Numerical and Experimental Frequency Response Results. Here, all Frequencies are in Hz.

	No Magnet			Small Magnet			Large Magnet		
	ω_l	ω_u	ω_u/ω_l	ω_l	ω_u	ω_u/ω_l	ω_l	ω_u	ω_u/ω_l
Analytical	40.1	88.8	2.21	38.7	80.9	2.09	37.4	78.8	2.11
Numerical	47.7	105.2	2.20	43.6	92	2.11	38.2	89.3	2.34
Experimental	52	110	2.11	46.1	100.4	2.18	39.1	100.4	2.57

4. CONCLUSIONS

First of all, eddy current damping (ECD) inclusion to the inertial amplification mechanism is successfully accomplished. By adjusting the distance between the ring magnet and the copper tube, damping strength is varied. Also the advantage of ECD is that it requires no external power source. With the inclusion of ECD, the vibration amplitudes in the four legged structure are suppressed in short amount of time compared to the case in which there is just structural damping. ECD constant found experimentally and numerically match quite well. On the other hand, analytically calculated damping constant differs due to the dipole approximation while calculating the magnetic field and magnetic flux of the ring magnet.

Secondly, a novel 1D locally resonant periodic structure is designed to generate a stop band at low frequencies. In order to analyze the periodic structure, a lumped parameter and a finite element model are generated. Within the unit cell of the periodic structure, two sets of spiral springs are used. Axial relative motion between the unit cells is accomplished by the parallel placement of these spiral springs. Parametric studies regarding the effect of mass distribution within the unit cell and the number of unit cells on the stop band characteristics are conducted. It is seen that when the main mass of the unit cell to resonator mass ratio is about one-third, the targeted stop band width is achieved. As the number of unit cells increases, deeper stop bands are obtained with the burden of increasing the overall size and mass of the periodic structure. Considering the compromise between stop band depth and mass of the periodic structure, four unit cells are chosen. Furthermore, ECD effect is included to the periodic structure through resonator masses being made of copper tubes in which ring magnets can vibrate. If the mass distribution within the unit cell is kept constant while the damping effect is increased, then slightly wider stop bands can be obtained. In order to attain the maximum ECD effect for the two different size ring magnets used in the analyses, an optimization study is performed. In this study, the copper tube mass and its inner radius are kept constant while its wall thickness and height are varied. Consequently, optimum geometry of the copper tube is determined. A

prototype of the locally resonant periodic structure including ECD is produced for experimental validation. During the assembly of the prototype, additional components are used within the unit cell for connection purposes. Their influence on the magnetic density and eddy current density are observed via electromagnetic FEA. It is seen that the stainless steel components in the vicinity of the ring magnet and copper tube decrease the ECD effect.

To sum up, ECD is implemented to an inertial amplification mechanism including four legged structure and to a 1D locally resonant periodic structure. ECD constant attained in both structures is obtained analytically, numerically and experimentally. For future work, non-magnetic materials can be used in order not to disturb the generated eddy currents in the copper tube.

REFERENCES

1. Gatti, P. L., *Applied Structural and Mechanical Vibrations: Theory and Methods*, CRC Press, 2014.

2. Rao, S. S. and F. F. Yap, *Mechanical vibrations*, Vol. 4, Addison-Wesley, New York, 1995.

3. Nashif, A. D., D. I. Jones and J. P. Henderson, *Vibration damping*, John Wiley & Sons, 1985.

4. Genta, G., *Vibration dynamics and control*, Springer, 2009.

5. Findeisen, D., *System dynamics and mechanical vibrations: an introduction*, Springer Science & Business Media, 2013.

6. Jones, D. I., *Handbook of viscoelastic vibration damping*, John Wiley & Sons, New York, 2001.

7. Priya, S. and D. J. Inman, *Energy harvesting technologies*, Vol. 21, Springer, New York, 2009.

8. Vidaurre, A., J. Riera, J. A. Monsoriu and M. H. Giménez, "Testing theoretical models of magnetic damping using an air track", *European Journal of Physics*, Vol. 29, No. 2, pp. 335–343, 2008.

9. Molina-Bolívar, J. and A. Abella-Palacios, "A laboratory activity on the eddy current brake", *European Journal of Physics*, Vol. 33, No. 3, pp. 697–707, 2012.

10. Wiederick, H., N. Gauthier, D. Campbell and P. Rochon, "Magnetic braking: Simple theory and experiment", *American Journal of Physics*, Vol. 55, No. 6, pp. 500–503, 1987.

11. Cadwell, L. H., "Magnetic damping: analysis of an eddy current brake using an airtrack", *American journal of physics*, Vol. 64, No. 7, pp. 917–923, 1996.

12. Bae, J.-S., M. K. Kwak and D. J. Inman, "Vibration suppression of a cantilever beam using eddy current damper", *Journal of Sound and Vibration*, Vol. 284, No. 3, pp. 805–824, 2005.

13. Sodano, H. A., J.-S. Bae, D. J. Inman and W. K. Belvin, "Concept and model of eddy current damper for vibration suppression of a beam", *Journal of Sound and Vibration*, Vol. 288, No. 4, pp. 1177–1196, 2005.

14. Elbuken, C., M. Khamesee and M. Yavuz, "Eddy current damping for magnetic levitation: downscaling from macro-to micro-levitation", *Journal of Physics D: Applied Physics*, Vol. 39, No. 18, pp. 3932–3938, 2006.

15. Ebrahimi, B., M. B. Khamesee and M. F. Golnaraghi, "Design and modeling of a magnetic shock absorber based on eddy current damping effect", *Journal of Sound and Vibration*, Vol. 315, No. 4, pp. 875–889, 2008.

16. Bae, J.-S., J.-H. Hwang, J.-H. Roh, J.-H. Kim, M.-S. Yi and J. H. Lim, "Vibration suppression of a cantilever beam using magnetically tuned-mass-damper", *Journal of Sound and Vibration*, Vol. 331, No. 26, pp. 5669–5684, 2012.

17. Zuo, L., X. Chen and S. Nayfeh, "Design and analysis of a new type of electromagnetic damper with increased energy density", *Journal of vibration and acoustics*, Vol. 133, No. 4, pp. 1–8, 2011.

18. Wang, Z., Z. Chen and J. Wang, "Feasibility study of a large scale tuned mass damper with eddy current damping mechanism", *Earthquake Engineering and Engineering Vibration*, Vol. 11, No. 3, pp. 391–401, 2012.

19. Jensen, J. S., "Phononic band gaps and vibrations in one-and two-dimensional mass-spring structures", *Journal of Sound and Vibration*, Vol. 266, No. 5, pp.

1053–1078, 2003.

20. Dilber, G., *Phononic band gaps in two-dimensional periodic structures with inertial amplification mechanisms*, Master's Thesis, Bogazici University, Turkey, 2012.

21. Wang, G., X. Wen, J. Wen and Y. Liu, "Quasi-one-dimensional periodic structure with locally resonant band gap", *Journal of Applied Mechanics*, Vol. 73, No. 1, pp. 167–170, 2006.

22. Wang, G., J. Wen and X. Wen, "Quasi one dimensional phononic crystals studied using the improved lumped mass method: Application to locally resonant beams with flexural wave band gap", *Physical Review B*, Vol. 71, No. 10, pp. 104–302, 2005.

23. Yu, D., Y. Liu, G. Wang, H. Zhao and J. Qiu, "Flexural vibration band gaps in Timoshenko beams with locally resonant structures", *Journal of Applied Physics*, Vol. 100, No. 12, pp. 1–5, 2006.

24. Liu, Y., D. Yu, L. Li, H. Zhao, J. Wen and X. Wen, "Design guidelines for flexural wave attenuation of slender beams with local resonators", *Physics Letters A*, Vol. 362, No. 5, pp. 344–347, 2007.

25. Xiao, Y., J. Wen, D. Yu and X. Wen, "Flexural wave propagation in beams with periodically attached vibration absorbers: Band-gap behavior and band formation mechanisms", *Journal of Sound and Vibration*, Vol. 332, No. 4, pp. 867–893, 2013.

26. Xiao, Y., J. Wen, L. Huang and X. Wen, "Analysis and experimental realization of locally resonant phononic plates carrying a periodic array of beam-like resonators", *Journal of Physics D: Applied Physics*, Vol. 47, No. 4, pp. 1–12, 2013.

27. Yilmaz, C., G. Hulbert and N. Kikuchi, "Phononic band gaps induced by inertial amplification in periodic media", *Physical Review B*, Vol. 76, No. 5, pp. 1–9, 2007.

28. Yilmaz, C. and G. Hulbert, "Theory of phononic gaps induced by inertial amplification in finite structures", *Physics Letters A*, Vol. 374, No. 34, pp. 3576–3584, 2010.

29. Acar, G. and C. Yilmaz, "Experimental and numerical evidence for the existence of wide and deep phononic gaps induced by inertial amplification in two-dimensional solid structures", *Journal of Sound and Vibration*, Vol. 332, No. 24, pp. 6389–6404, 2013.

30. Saslow, W., "Maxwell's theory of eddy currents in thin conducting sheets, and applications to electromagnetic shielding and MAGLEV", *American Journal of Physics*, Vol. 60, No. 8, pp. 693–711, 1992.

31. Bistafa, S. R., "On the derivation of the terminal velocity for the falling magnet from dimensional analysis", *Revista Brasileira de Ensino de Física*, Vol. 34, No. 2, pp. 1–4, 2012.

32. Pelesko, J. A., M. Cesky and S. Huertas, "Lenz's law and dimensional analysis", *American journal of physics*, Vol. 73, No. 1, pp. 37–39, 2005.

33. Bae, J.-S., J.-H. Hwang, J.-S. Park and D.-G. Kwag, "Modeling and experiments on eddy current damping caused by a permanent magnet in a conductive tube", *Journal of mechanical science and technology*, Vol. 23, No. 11, pp. 3024–3035, 2009.

34. Donoso, G., C. Ladera and P. Martin, "Magnet fall inside a conductive pipe: motion and the role of the pipe wall thickness", *European Journal of Physics*, Vol. 30, No. 4, pp. 855–868, 2009.

35. Donoso, G., C. L. Ladera and P. Martín, "Damped fall of magnets inside a conducting pipe", *American Journal of Physics*, Vol. 79, No. 2, pp. 193–200, 2011.

36. Partovi, M. H. and E. J. Morris, "Electrodynamics of a magnet moving through a conducting pipe", *Canadian journal of physics*, Vol. 84, No. 4, pp. 253–271, 2006.

37. Irvine, B., M. Kemnetz, A. Gangopadhyaya and T. Ruubel, "Magnet traveling through a conducting pipe: A variation on the analytical approach", *American Journal of Physics*, Vol. 82, No. 4, pp. 273–279, 2014.

38. Uhlig, R. P., M. Zec, H. Brauer and A. Thess, "Lorentz force eddy current testing: a prototype model", *Journal of Nondestructive Evaluation*, Vol. 31, No. 4, pp. 357–372, 2012.

39. Derby, N. and S. Olbert, "Cylindrical magnets and ideal solenoids", *American Journal of Physics*, Vol. 78, No. 3, pp. 229–235, 2010.

40. MacLatchy, C. S., P. Backman and L. Bogan, "A quantitative magnetic braking experiment", *American Journal of Physics*, Vol. 61, No. 12, pp. 1096–1101, 1993.

41. Hahn, K. D., E. M. Johnson, A. Brokken and S. Baldwin, "Eddy current damping of a magnet moving through a pipe", *American Journal of Physics*, Vol. 66, No. 12, pp. 1066–1076, 1998.

42. Cheah, S. K. and H. A. Sodano, "Novel eddy current damping mechanism for passive magnetic bearings", *Journal of Vibration and Control*, Vol. 14, No. 11, pp. 1749–1766, 2008.

43. Camacho, J. and V. Sosa, "Alternative method to calculate the magnetic field of permanent magnets with azimuthal symmetry", *Revista mexicana de física E*, Vol. 59, No. 1, pp. 8–17, 2013.

44. Levin, Y., F. L. da Silveira and F. B. Rizzato, "Electromagnetic braking: A simple quantitative model", *Am. J. Phy.*, Vol. 74, No. 9, pp. 815–817, 2006.

45. Inman, D. J. and R. C. Singh, *Engineering vibration*, Vol. 3, Prentice Hall, 2001.

46. Pestel, E. and F. Leckie, *Matrix methods in elastomechanics*, Vol. 435, McGraw-Hill, 1963.

47. Broch, J. T., *Mechanical vibration and shock measurements*, Brüel & Kjær, Naerum, 1980.

48. Brillouin, L., *Wave propagation in periodic structures: electric filters and crystal lattices*, Courier Corporation, 2003.

49. Singh, R. and V. Singh, "Analysis of Eddy current damper for suppression of vibrations using COMSOL software", *Engineering Solid Mechanics*, Vol. 3, No. 4, pp. 215–222, 2015.

50. Kim, J.-H., Y.-G. Lee and C.-G. Kim, "An experimental study on a new air-eddy current damper for application in low-frequency accelerometers", *Journal of Mechanical Science and Technology*, Vol. 29, No. 9, pp. 3617–3625, 2015.